

XAI Model for Accurate and Interpretable Landslide Susceptibility

K. Youssef^{1,5*}, K. Shao^{2*}, S. Moon², L.-S. Bouchard^{1,3,4}

¹Department of Chemistry and Biochemistry, University of California Los Angeles, 607 Charles E. Young Dr. East, Los Angeles, CA 90095-1569, USA.

²Department of Earth, Planetary, and Space Sciences, University of California, Los Angeles, 595 Charles E. Young Dr. East, Los Angeles, CA 90095-1567

³Department of Bioengineering, University of California Los Angeles, 607 Charles E. Young Dr. East, Los Angeles, CA 90095-1569, USA.

⁴California NanoSystems Institute, University of California Los Angeles, 607 Charles E. Young Dr. East, Los Angeles, CA 90095-1569, USA.

⁵Current address: Biomedical Imaging Research Institution, Cedars-Sinai Medical Center, 116 N Robertson Blvd, Los Angeles, CA 90048, USA.

* co-first authors

Abstract. Landslides are notoriously difficult to predict. Deep neural networks (DNNs) models are more accurate than statistical models. However, they are uninterpretable, making it difficult to extract mechanistic information about landslide controls in the modeled region. We developed an explainable AI (XAI) model to assess landslide susceptibility that is computationally simple and features high accuracy. We validated it on three different regions of eastern Himalaya that are highly susceptible to landslides. SNNs are computationally much simpler than DNNs, yet achieve similar performance while offering insights regarding the relative importance of landslide control factors in each region. Our analysis highlighted the importance of: 1) the product of slope and precipitation rate and 2) topographic aspects that contribute to high susceptibility in landslide areas. These identified controls suggest that strong slope-climate couplings, along with microclimates, play more dominant roles in eastern Himalayan landslides. The model outperforms physically-based stability and statistical models.

1 Introduction

Landslides are a major natural hazard that cause billions of dollars in direct damages and thousands of deaths globally each year (Petley, 2012; Froude & Petley, 2018). Landslides can also cause various secondary hazards, such as damming and flooding, which often leave a region prone to subsequent damage following the initial event. (R. Huang & Fan, 2013) Additionally, landslide debris may cause instability by perturbing river sedimentation and disrupting ecosystems (Fan et al., 2019; R. Huang & Fan, 2013). As landslide hazards are expected to increase due to climate change, scientists have sought to more accurately measure landslide susceptibility (Tien Bui et al., 2012, 2019; Phong et al., 2019; Dikshit et al., 2020; Kirschbaum et al., 2020; Stanley & Kirschbaum, 2017), an estimate of the probability that a landslide may occur in a specific area, with the goal of mitigating its impact on the economy, safety, and local ecosystems.

Landslide occurrences are affected by various factors including physical attributes of the terrain, such as topographic slopes and drainage areas, and material properties such as the density and strength of soil and bedrock (Dietrich et al., 1995; Montgomery & Dietrich, 1994; Montgomery et al., 1998; Radbruch-Hall, 1982). Also, environmental conditions such as climate, hydrology, ecology, and ground motion due to earthquakes

Corresponding authors: S.G. Moon, L.-S. Bouchard, sgmoon@ucla.edu, lsbouchard@ucla.edu

play an important role in causing slope instability (Guzzetti et al., 1999; Baum et al., 2002; Meunier et al., 2008a). Landslide susceptibility is calculated from these various controlling factors either through physically based models (Montgomery & Dietrich, 1994; Montgomery et al., 1998; Baum et al., 2002, 2010), data-driven approaches utilizing statistical analysis (Lee & Sambath, 2006; Regmi et al., 2014), or machine learning techniques (ML), including support vector machines and deep neural networks (Tien Bui et al., 2019; Van Dao et al., 2020; Tien Bui et al., 2020; Conforti et al., 2014; Gómez & Kavzoglu, 2005; Lee et al., 2004).

While substantial work has been devoted to assessing susceptibility, each model has shortcomings. Physically- or mechanistically-based approaches, built on limit equilibrium between driving and resisting forces, have been widely applied to assess slope stability over a region (Montgomery & Dietrich, 1994; Dietrich et al., 1995; Montgomery et al., 1998; Dietrich et al., 2001). However, mechanistic models have limitations, including a limited number of variables, simplified assumptions of certain environmental conditions (e.g., antecedent moistures, bedrock structure) and landslide geometry, or the high cost of geotechnical exploration (Guzzetti et al., 1999). Alternatively, data-driven approaches, including statistical and ML methods, can handle a large number of controls to assess susceptibility. Statistical methods such as logistic regression and likelihood ratios (Lee & Sambath, 2006; Regmi et al., 2014; Reichenbach et al., 2018) can utilize a multitude of landslide controls as inputs. Scientists using these data-driven approaches have obtained a measurable degree of success in determining areas susceptible to landslides (Lee & Sambath, 2006; Regmi et al., 2014; Tien Bui et al., 2019). However, these data-driven models rely on the expert’s choice, preconditions, and classifications of input variables. The outcome of these models’ results, the landslide susceptibility map, does not decouple individual feature contributions to landslide susceptibility nor account for their interdependencies due to the limited computational capabilities in conventional approaches (Reichenbach et al., 2018).

Machine learning approaches such as fuzzy logic algorithms, support vector machines, and DNNs have been applied to landslide studies for mapping landslide susceptibility (Pradhan, 2013; Tien Bui et al., 2020; Gómez & Kavzoglu, 2005). DNNs have achieved superior performance compared to both statistical methods and other ML approaches due to their use of nonlinearities, complex interdependencies of interlayer connections, as well as internal representations of data (Conforti et al., 2014; Gómez & Kavzoglu, 2005; Tien Bui et al., 2020; Van Dao et al., 2020; Rudin, 2019; Gunning et al., 2019; Adadi & Berrada, 2018). However, the “black box” nature of DNNs has been a major hurdle for their adoption in practice and research, making it difficult for experts to understand and trust the outcome. With DNNs it is nearly impossible to determine the exact relation between individual inputs and outputs (Rudin, 2019; Gunning et al., 2019; Adadi & Berrada, 2018). Lack of interpretability is a weakness of DNNs and a fundamental drawback for high-stakes applications such as landslide mitigation where decisions impact lives and result in untold costs of insurance and reconstruction (Cui et al., 2019; Froude & Petley, 2018; R. Huang & Fan, 2013).

The DNN’s lack of interpretability has prompted Defense Advanced Research Projects Agency (DARPA)’s third wave of AI call in 2017 and the European Union’s 2018 General Data Protection Regulation, which grants a “right to an explanation,” for algorithmic decisions that are made (European Commission, 2020). Next-generation AI systems refers to the so-called explainable or interpretable AI (XAI) models. The latter must be able to construct explanatory models for classes of real-world phenomena that can be communicated to humans (Adadi & Berrada, 2018). Various XAI categories have since been defined in the literature based on factors such as application and methodology, where each category is further divided into subclasses (Li et al., 2020). Although the use of XAI in research is expanding, existing approaches aimed at

explaining black box models exhibit a trade-off between accuracy and interpretability, resulting in a large gap in performance. Recently, Rudin (Rudin, 2019) showed that with proper feature engineering, and a shift from explaining existing black box models to creating methods with inherently interpretable models, the trade-off between accuracy and interpretability can be circumvented.

There is an urgent need for XAI methods in the analysis of geohazards (Bergen et al., 2019; Toms et al., 2020; Dikshit et al., 2020). At this time, none exist specifically for the modeling of landslide hazards. Thus, we developed a novel end-to-end method that bridges the gap between explainability and accuracy. Our XAI method, termed superposable neural network (SNN), is data-driven, in the sense that explanations are generated purely from the data without external information, hardwired physical relationship, or preconditioning. It is a hybrid between model extraction methods and feature-based methods. Model extraction methods aim to train an explainable “student” model to mimic the behavior of a “teacher” model, which is taken here to be a high performing pre-trained black box model (Li et al., 2020). On the other hand, feature-based methods aim to analyze the influence or the importance of input features (Li et al., 2020).

2 Data and Methods

2.1 Superposable neural networks

Our XAI model is an additive neural network architecture enforcing no interconnections between inputs. The lack of interconnections between features is what enables explainability. Additive models have been gaining increasing interest in XAI (Agarwal et al., 2020; Hastie & Tibshirani, 1990; Friedman, 2001), where separate neural networks each specialized in a single feature are combined to optimize a common outcome. Such models enable determining the contribution of each input feature to the final outcome. However, state-of-the-art algorithms rely on gradient descent-based optimizers to obtain model parameters, making them notoriously difficult to train jointly and expand beyond a limited number of features. Herein we introduce a new training approach that enables the separate training of individual neural networks. Our approach utilizes several state-of-the-art ML techniques (multi stage training, knowledge distillation, second order optimization (Youssef et al., 2015; Bouchard & Youssef, 2018; Youssef et al., 2018a; Yu & Wilamowski, 2011; Hinton et al., 2015)) to deliver a model that is optimal in terms of performance and remarkably simple in terms of architecture.

In the superposable neural network (SNN; Figs. 1 and S1), instead of interdependencies being embedded in layers of network connections, interdependencies are explicitly created as a product function of multiple original input features, which we refer to as composite features. An automated feature selection method finds interdependencies between features prior to training the network by isolating composite features that contribute to the desired outcome. Contributing composite features are explicitly added as independent inputs to the model, while non-contributing composite features are discarded (see Supporting Information).

Composite features are categorized by the number of product operations involved. For example, given a problem with n original input features x_1, x_2, \dots, x_n , we can generate a set of $M \geq n$ composite features $\chi_1, \chi_2, \dots, \chi_M$, where Level-1 features are merely the single original features (first-degree monomials such as x_i). Level-2 features are composite features defined as the product of two first-degree monomials. As an example, we may form the product $x_1 * x_2$ (second-degree monomial), where the monomials x_1 and x_2 are Level-1 features. Level-3 features are composite features consisting of a product of three first-degree monomials, such as $x_1 * x_2 * x_3$ or $x_1 * x_2^2$, and so on, resulting in third-degree monomials. Composite features are restricted to

functions that cannot be derived from another function by elementary algebraic transformations. For example, $x_1^2 * x_2^2$ and $2 * x_1 * x_2$ are not permitted since they can be derived from $x_1 * x_2$ by elementary operations (namely, by squaring and scaling, respectively). Using composite features, SNNs can approximate any continuous function for inputs within a specific range as a polynomial expansion to any desired precision, giving SNNs the ability to retain a level of accuracy on par with state-of-the-art DNNs. While this architecture results in outputs where the contributions from each input feature can be separated, we are left with the non-trivial question of how can one train such a deceptively simple SNN to yield high performance on par with state-of-the-art deep nets. The latter are orders of magnitude more complex in terms of number of parameters and connectivity, making the training of SNNs appear to be impossible.

The SNN is represented mathematically by the function (Eq. 2):

$$S_t(\{\chi_j\}) = \sum_j \left(\sum_k w_{j,k} e^{-(a_{j,k}\chi_j + b_{j,k})^2} + c_j \right). \quad (1)$$

It contains only two hidden layers of neurons with radial basis activation functions in the first layer and linear activation functions in the second layer. The choice of radial basis activation functions allows the user to minimize the number of neurons in the model, which is critically important for maximizing the efficiency of our method. Each input χ_j is exclusively connected to a group of neurons to form an independent function $S_j = \sum_k w_{j,k} e^{-(a_{j,k}\chi_j + b_{j,k})^2} + c_j$ and the SNN output $S_t = \sum_j S_j$ is the sum of all independent functions, where $j = 1 : \text{number of features } (m)$, $k = 1 : v$, the number of neurons per feature, and χ_j is the j^{th} composite feature. In addition to determining the features and interdependencies between features that contribute to the outcome, the SNN architecture enables the quantification of the exact contribution of each feature and feature interdependency to the outcome.

Using second-order optimization in lieu of the commonly used gradient based first-order optimization is a key factor in minimizing model complexity and maximizing accuracy in our method. Second-order optimization is more robust with respect to hyperparameter tuning, and offers better accuracy, convergence speed, and efficiency (Ozyildirim & Kiran, 2020; Le et al., 2011; Battiti, 1992; H. Tan & Lim, 2019; Montavon et al., 2012; Yu & Wilamowski, 2011; Wilamowski & Yu, 2010). However, second-order optimization is not commonly used due to the high computational and memory storage costs involved. In previous studies, we have tackled this problem by developing the multistage trained (MST) DNN (Youssef et al., 2015; Bouchard & Youssef, 2018; Youssef et al., 2018a). MST is a special type of deep net consisting of smaller subunits that are trained in hierarchical fashion using second order optimizers. MSTs employ a hierarchical structure of multilayer perceptrons, each trained in successive stages, enabling a better solution to be obtained, requiring only modest compute resources (Youssef et al., 2015; Bouchard & Youssef, 2018; Youssef et al., 2018a).

In this work, a second-order MST DNN (Youssef et al., 2015; Bouchard & Youssef, 2018; Youssef et al., 2018a) is used as the teacher model of the SNN. Two stages of knowledge distillation implemented in a step-wise manner are used to further facilitate the optimization of the highly constrained SNN architecture in a way that maximizes accuracy while minimizing the number of neurons for optimal explainability. The robustness characteristic of second-order optimization is key to enabling the automation of our feature selection method, which involves training thousands of DNN models. This would not have been possible with first-order optimization due to the high sensitivity to hyperparameters and the manual effort involved in tuning. SNNs based on knowledge distillation and second-order optimization techniques aim to deliver an explainable neural network model without compromising accuracy (see details in Supporting Information).

2.2 Study Area

Asia holds the majority of human losses due to landslides globally, with a high concentration in the Himalayan Arc (Petley, 2012; Froude & Petley, 2018). Previous studies in the Himalaya regions presented various controlling factors for landslides, which include steep slopes, extreme precipitation events, flooding, and frequent earthquakes (Larsen & Montgomery, 2012; Coudurier-Curveur et al., 2020; Bookhagen & Burbank, 2010; Chowdhuri et al., 2021; Kent & Dasgupta, 2004). The eastern end of Himalaya has numerous landslides, which may be affected by extreme precipitation events or earthquakes from active tectonics (Figs. 2, S2). This area exhibits a dramatic precipitation gradient due to moisture originating from the Bay of Bengal in the south (Bookhagen & Burbank, 2010; Barros et al., 2004; Yang et al., 2018) (Fig. S3). Mean annual precipitation rates (*MAP*) vary from ~ 7000 mm/yr in the rangefront to ~ 200 mm/yr in the hinterland (Bookhagen & Burbank, 2010). The number of extreme rainfall events (*NEE*) calculated as the number of days that exceed the 90th percentile of daily rainfall rates, reaches ~ 13 and ~ 2 events/yr in the rangefront and hinterland, respectively (Bookhagen & Burbank, 2010). Both daily and mean annual precipitation rates are calculated based on 3-h measurements from the Tropical Rainfall Measuring Mission (TRMM) 2B31 over 12 years (January 1998 to December 2009), with a spatial resolution of ~ 2.6 km (Bookhagen & Burbank, 2010). Orographic patterns of precipitation rates and variability are also observed in the 57-yr Asian Precipitation-Highly Resolved Observational Data Integration Towards Evaluation of Water Resources project (APHRODITE) (Yatagai et al., 2012). In addition, this area has consistently steep slopes (>0.59), from the rangefront, where Holocene Himalayan shortening is concentrated near and along the Main Frontal Thrust, into the hinterland, which is affected by deglaciations from the last glacial maximum (Burgess et al., 2012; Haproff et al., 2019, 2020; Salvi et al., 2020). Furthermore, the area is prone to active seismicity. The 1950 M_s 8.6 Assam earthquake, one of the largest earthquakes in the Himalayan range, struck near the Namche Barwa region (Ben-Menahem et al., 1974). Additionally, the eastern end of Himalaya has experienced >450 earthquakes with $M > 4$ since 1973 according to Incorporated Research Institutions for Seismology data archive (www.iris.edu, accessed on 10/01/2020).

We selected three regions (N-S, NW-SE, and E-W regions) within the eastern end of Himalaya that have varying ranges of landslide controls to test the performance of the SNN model (Figs. S2, S4). Both the N-S and E-W regions extend from the active rangefront to the hinterland, from north to south and east to west, respectively. The NW-SE region mostly lies along the active rangefront. Testing the SNN over three regions will allow us to examine the following: 1) whether there are universal or distinctly different controls of landslides; and 2) whether SNN-determined independent functions of feature contributions to susceptibility, $\{S_j\}$, are similar across these three regions.

2.3 Landslide Inventory

We generated a landslide inventory of the eastern end of Himalaya by combining manual delineation by detecting vegetation changes with a semi-automatic detection algorithm (Ghorbanzadeh et al., 2019; Prakash et al., 2020). We used 30 m resolution Landsat 8 imagery from November 2017 with bands 2, 3, 4, 5, and 7. (United States Geological Survey EarthExplorer, 2020) These satellite images were used to generate natural and false color imagery to best identify landslides. High degrees of vegetation in the area allow for clear delineation of landslides suitable for mapping. Then, landslide polygon detection and delineation were mainly based on Landsat spectral signatures, with consideration for topographic and climatic information such as slope, relief, and *MAP* in an automatic detection algorithm (Krizhevsky et al., 2012; Lawrence et al., 1997; Ghorbanzadeh et al., 2019; Prakash et al., 2020). Next, the output from the

automatic detection algorithm was visually compared with Landsat 8 imagery, high-resolution Google Earth images, and a 4-band Planetscope Scene with a 3 m resolution. We manually corrected landslides from the automatic detection method to resolve common problems such as the inaccurate representation of landslide areas because of aggregated features and small detected features that are not related to landslides (Marc & Hovius, 2015; Parker et al., 2011). We used the manually corrected, automatically mapped landslides as our final landslide inventory (details in Supporting Information).

Our landslide inventory covers our overall study area of 4.19×10^9 m² and has 2,289 landslides whose areas range from 900 to 1.96×10^6 m². Landslide densities calculated over a 2.25 km² window are high in the rangefront (maximum of 0.121) and low in the hinterland (maximum of 0.039) (Fig. 2). The area-frequency distribution of landslides is similar to a previous study from a nearby region (Larsen & Montgomery, 2012) (Fig. S3). They showed that a transition from soil to bedrock landslides occur at a landslide area of $\sim 100,000$ m² (Larsen et al., 2010; Larsen & Montgomery, 2012). In our landslide inventory, <1% of landslides in numbers and <20% of total landslide area are greater than 100,000 m² (Table S1). Thus, most of the mapped landslides are likely soil landslides. The spatial distributions and extents of landslides from our inventory are shown in Fig. 1a, Figs. S5a and S6a, for the N-S, NW-SE, and E-W regions, respectively. Landslide density is calculated within a 2.25 km² window, which is greater than the largest landslide size (1.95 km²) (Fig. 2).

2.4 Feature Descriptions

We quantified the spatial distribution of 15 topographic, climatic, and geologic controls and used them as input features for SNN. The 15 single features include topographic controls of aspect (*Asp*), mean curvature (*Curv_M*), planform curvature, profile curvature, total curvature, distance to channel (*Dist_C*), drainage area, elevation (*Elev*), local relief calculated as an elevation range within a 2.5 km radius circular window (*Relief*), and slope, climatic or hydrologic controls of discharge, mean annual precipitation (*MAP*), and number of extreme events (*NEE*), and geologic controls of distance to lithologic boundaries (i.e., mostly faults) (*Dist_F*) and distance to the Main Frontal Thrust and suture zone (*Dist_{MFT}*). These features were selected from literatures that examine landslide occurrences in the Himalayan region (Devkota et al., 2013; Regmi et al., 2014; Mandal & Mandal, 2018; Chowdhuri et al., 2021). We mostly used features directly measured through satellite data such as the 90 m digital elevation model from the Shuttle Radar Topography Mission (SRTM) (United States Geological Survey EarthExplorer, 2020), rainfall rates and variability from TRMM (Bookhagen & Burbank, 2010), and published geologic maps (Haproff et al., 2019; Taylor & Yin, 2009). Utilizing the open-source satellite data with a long-term historic archive allows our approach to be easily implemented in other regions (e.g., Himalayan Arc) with limited accessibility, high landslide potential, and long landslide histories (Zhu et al., 2019; Petley, 2012; Froude & Petley, 2018; Kirschbaum et al., 2020). The details of our data sources and methods of calculation as well as the uncertainties and limitations of our study are explained in the Supporting Information (Fig. S3, Table S2).

2.5 Assessments of Model Performances

A threshold value of S_t can be used as a binary classifier to predict landslides and compare them with observed landslides from our inventory. We selected a threshold susceptibility corresponding to the closest point to a perfect classifying model of a 100% true positive rate and 0% false positive rate in a receiver operating characteristic (ROC) curve. Areas with S_t greater and lower than this threshold are classified as landslide (*ld*) and non-landslide (*nld*) areas, respectively, in model. We used the threshold S_t values of 0.406, 0.519, and 0.572, for the N-S, NW-SE, and E-W regions, respectively.

We assessed SNN performance based on various metrics including area under the receiver operating characteristic curve (AUROC) and success rate curve. In addition, we calculated the statistical measures of accuracy, sensitivity (probability of detection, POD), specificity (probability of false detection, POFD), and POD-POFD. The performance and explainability of the SNN were compared with results from 1) a physically-based model (SHALSTAB) suitable for soil landslides, which are the dominant landslide type in the region (Montgomery & Dietrich, 1994; Dietrich et al., 2001; Moon et al., 2011; Larsen & Montgomery, 2012); 2) the most commonly used statistical models, logistic regression and likelihood ratios (Lee, 2005; Akgun, 2012; Reichenbach et al., 2018); and 3) a conventional deep net trained using the adaptive moment estimation (Adam) optimizer (Kingma & Ba, 2014). We also calculated the 95% confidence interval of mean AUROC from the statistical and neural network model outputs based on a 10-fold cross validation (details in Supplemental Information).

2.6 Identifying Landslide Controls and Quantifying Their Contributions

We used our SNN outputs to better understand the relative importance of controlling factors and their functional relationships with landslide susceptibility. By utilizing the exact contribution of S_j from each feature at the pixel scale, we quantified the relative importance of landslide controls vary in different localities. We identified primary controls of landslides that induce large differences in average S_j between (*ld*) and (*nld*) areas (i.e., $\Delta\bar{S}_j = \bar{S}_{j,ls} - \bar{S}_{j,nls}$) within a given area (e.g., 2.25 km²) (Fig. 2, Figs. S5, S6). Additionally, we calculated $\Delta\bar{S}_j$ using observed landslide and non-landslide areas from our inventory to compare with those from our SNN-predicted landslides. Both results show similar rankings and magnitudes of $\Delta\bar{S}_j$ in our studied regions (Fig. 2d-e, Figs. S5d, S6d). For comparison, we also identified primary controls of landslides and their relative contributions from SNN-Level1 and the weights determined by the logistic regression model (Figs. S7, S8). Lastly, we examined the independent functions $\{S_j\}$ to better understand the controls of individual features on landslide susceptibility. The details of our methods are explained in the Supporting Information.

3 Results

The SNN model performance is comparable to that of second-order-optimized DNNs, while providing a significant improvement over commonly used physically-based model, statistical models, and first-order-optimized DNNs (Tables S3). AUROCs of Level-1 and Level-2 SNNs are 0.864 and 0.896 (N-S), 0.826 and 0.856 (NW-SE), and 0.878 and 0.919 (E-W), with Level-2 SNNs capturing over 98% of the teacher model (MST) performance across all three study regions. Additionally, we tested Level-3 SNN in one of the regions (NW-SE) and found it to perform marginally better (~1%) than Level-2 SNN. Given that the performance of Level-2 already exceeds 98% of the teacher model’s performance, we adopt the Level-2 SNN for this study. The Level-2 SNN is optimal in the sense that it provides high accuracy (comparable to deep nets) and relatively simple model complexity (hereafter, SNN refers to Level-2 SNN). Our SNN shows a statistically significant improvement over a conventional DNN (AUROC = 0.837 (N-S), 0.762 (NW-SE), 0.835 (E-W)). The SNN achieved 19-23% improvement in AUROC over the top performing single original features of *MAP* or slope (AUROC = 0.756 (N-S) or 0.696 (NW-SE) and 0.760 (E-W), respectively), 19-26% improvement over a physically-based model (SHALSTAB) (AUROC = 0.756 (N-S), 0.694 (NW-SE), 0.732 (E-W)), 3-10% improvement over logistic regression (AUROC = 0.869 (N-S), 0.795 (NW-SE), 0.880 (E-W)) and likelihood ratios (AUROC = 0.841 (N-S), 0.792 (NW-SE), 0.835 (E-W)) in our three study regions. The 95% confidence intervals of the mean AUROC of the SNN lie above and do not overlap with those of the statistical models and DNN (Tables S4). In addition, other performance metrics such as accuracy,

POD, POFD, and POD-POFD from the SNN are improved over other methods as well (Tables S5).

We identify *composite features* as locally important landslide controls on our study area. Namely, the product of slope times *NEE* or *MAP*, and *Asp* (Fig. 2c, d). The primary control of *MAP*Slope* and *NEE*Slope* is consistent among our three study regions in the eastern end of Himalaya (Fig. 2c, Figs. S5c, S6c) despite differences in the spatial distribution and magnitude of precipitation and proximity to a major fault with a history of earthquakes (Fig. S4). The overall importance of slope and climatic features identified by the SNN are similar to those inferred from the weights determined by logistic regression. However, the relative and absolute importance of features decoupled from other features by the SNN are different from those determined by logistic regression (Fig. S7). We note that the model performances obtained here cannot be directly compared to DNN performances cited in the literature because these models are trained on different regions; this is why independent validation against competing methods are provided here over the same region.

To assess the relative importance between climate and slope features, we used the SNN Level-1 results. We first add all single original features' $\Delta\bar{S}_j$ related to climate ($j = Asp, NEE, MAP$) (hereafter, $\Delta\bar{S}_{climate}$) and compared it to that of slope, $\Delta\bar{S}_{Slope}$, for a given area. Average ($\pm 1\sigma$) $\Delta\bar{S}_{climate}$ and $\Delta\bar{S}_{Slope}$ values are 0.044 ± 0.028 and 0.052 ± 0.050 (N-S), 0.042 ± 0.024 and 0.052 ± 0.040 (NW-SE), and 0.031 ± 0.023 and 0.059 ± 0.040 (E-W), respectively. Interestingly, $|\Delta\bar{S}_{climate}|$ exceeds $|\Delta\bar{S}_{Slope}|$ in $\sim 59\%$, $\sim 53\%$, and $\sim 38\%$ of localities, which encompass $\sim 84\%$, $\sim 60\%$, and $\sim 59\%$ of landslide areas in the N-S, NW-SE, and E-W regions, respectively (Fig. S8). We find that the importance of climate feature contributions to landslide occurrence can exceed that of slope by ~ 30 times in certain locations and in most localities with high landslide density.

The SNN-determined independent functions $\{S_j\}$ show varying relationships between features, feature interdependencies, and both their absolute susceptibility contribution (Fig. 3, Figs. S9, S10). $S_{MAP*Slope}$, $S_{NEE*Slope}$, and $S_{Elev*Slope}$ generally exhibit steep increases with feature value, followed by asymptotic behavior for the former two (Fig. 3a, Figs. S9a, S10a). The nonlinear relationships between landslide susceptibility and the product of slope and climatic features of *MAP* and *NEE* are similar to the predicted patterns of slope stability controlled by subsurface saturation (Supporting Information). In addition, S_{Asp} shows a peak around 145° , to 180° , indicating a preference for south-facing slopes, likely due to moisture from the Bay of Bengal (Bookhagen & Burbank, 2010) (Fig. 3b, Supporting Information). These functional relationships are similar to those deduced by the statistical method of likelihood ratios (*LR*) that represent the likelihood of landslide occurrence. However, unlike likelihood ratios, which assume the same, average likelihood ($LR = 1$) for each feature, S_j corresponding to $LR = 1$ varies depending on a feature's absolute, decoupled contribution to landslide susceptibility.

4 Discussion

Whereas explainable AI efforts involve a trade-off between accuracy and interpretability, the new SNN does not compromise accuracy. Given the SNN's inherent and unique ability to decouple individual feature contributions and select feature interdependencies, we can easily isolate the local contributions from primary controls discovered by the SNN (Fig. 2). Our local analyses for assessing landslide controls indicate that the contribution of climate features, such as *NEE*, *MAP*, and *Asp*, to landslide susceptibility tends to surpass that of slope for a majority of landslide occurrences in this area. Our findings are different from previous studies in other Himalayan regions that emphasize the dominance of tectonic and topographic contributions to erosional

processes (Coudurier-Curveur et al., 2020; Scherler et al., 2014). Our study highlights a prevalent climatic control on landslide occurrences in the eastern Himalayan region. Due to the eastward increasing trends of precipitation rate and variability along the Himalayas, the eastern end of Himalaya contains one of the largest strike-perpendicular climatic variations across the steep mountain range (Bookhagen & Burbank, 2010). This considerable climate gradient in the eastern end of Himalaya likely impacts landslide susceptibility.

The transparency of our XAI model offers insight into controlling factors of landslides while offering an accurate quantification of susceptibility. Specifically, SNNs highlighted important, yet under-appreciated controls of $NEE*Slope$, $MAP*Slope$, and Asp in our study site. The multiplication of two Level-1 features produces a Level-2 feature that measures the importance of both features. These controls of the product between slope and precipitation rates and intensity as well as aspect imply that landslides are affected by strong slope-climate *couplings* and aspect-related microclimates. The nonlinear asymptotic function of $S_{MAP*Slope}$ and $S_{NEE*Slope}$ can be explained by a physical mechanism of rainfall-induced landslide that induces slope failure due to an increase in pore-water pressure and subsurface saturation (Iverson, 2000) (details in Supporting Information). However, this deduced relation is different from observations of earthquake-induced landslide occurrences that increase nonlinearly with increasing slope (Meunier et al., 2008b; A.-L. Huang & Montgomery, 2014). The identified controls of MAP , NEE , and Asp imply that local precipitation infiltration affected by the spatial patterns of precipitation rates as well as moisture availability on steep slopes may be the dominant contributors to subsurface saturation in the eastern end of Himalaya (Supporting Information).

Identifying the exact trigger for a landslide requires dense measurements and historic records of the soil, hydrologic, and climatic conditions (e.g., soil moisture, antecedent rainfall, rainfall intensity) (Orland et al., 2020; Kirschbaum et al., 2020), which are often difficult to obtain, especially in rural mountainous areas with limited accessibility. We have shown that our SNN model can identify key controls and quantify their potential contributions to susceptibility, highlighting the essence of strong slope-climate coupled controls on landslide occurrences. The composite features identified by the SNN such as $NEE*Slope$ or $MAP*Slope$ are consistent with previous understanding of landslide mechanisms (Supporting Information). However, they were not explicitly implemented in previous data-driven statistical models. In DNNs, such couplings were likely identified, but if that were the case, the information would have been implicitly contained in the network weights and not readily available to the user. By incorporating the climatic controls from $MAP*Slope$ and Asp in the N-S region, the performance of the SNN improved, increasing AUROC by 3–26% compared to those of statistical or physically-based models (Montgomery & Dietrich, 1994; Dietrich et al., 2001; Lee, 2005; Akgun, 2012) (Supporting Information). This performance enhancement is substantial and could impact decisions regarding landslide hazards.

Our work presents a significant advance in XAI applications to natural hazards and circumventing the “black box” nature of common AI models. SNNs provide quantitative analysis of the controlling factors and further highlight the important, mechanistic interpretation of landslides. Our new approach based on tournament ranking and knowledge distillation provides a comprehensive framework that allows the user to examine numerous composite features, identify key controls, and more accurately model landslide susceptibility. As natural perturbations increase due to urban development and climate change, the SNN may provide a promising, data-driven predictive tool that will enable communities to tailor plans for hazard mitigation.

We note that our study has limitations. For one, our landslide and original feature data from the eastern end of Himalaya have relatively coarse resolutions and are temporally limited (e.g., 30 m resolution Landsat satellite images from 2017 (United

States Geological Survey EarthExplorer, 2020), 90 m resolution SRTM DEM (United States Geological Survey EarthExplorer, 2020), and ~ 2.6 km resolution TRMM data over 12 years (Bookhagen & Burbank, 2010)) (see details in Supporting Information). Due to the extremely rugged mountains in the Himalayas, the highest available DEM resolution without extensive data gaps, suitable for regional-scale landslide susceptibility analysis, is 90 m (Kirschbaum et al., 2020; Stanley & Kirschbaum, 2017). Also, there are no readily available time-series precipitation data with a resolution < 2.6 km in this area. Our study site doesn't have detailed information on high-resolution topography, surface materials (e.g., soil depth, bedrock structures), and climatic and ecohydrologic conditions (e.g., landslide-triggering storm intensity, vegetation types). Thus, our results from both physically-based or data-driven models may be biased due to the inherited uncertainties and limitations of our input data and may change when sufficient data become available (Leonarduzzi et al., 2021).

Despite data limitations and uncertainties, our SNN analysis of the eastern end of Himalaya presents an important contribution to landslide hazard studies. High mountains in Asia hold the majority of human losses due to landslides globally, with a high concentration in the Himalayan Arc, according to a global analysis conducted using 2004 - 2016 data (Petley, 2012; Froude & Petley, 2018). Due to the associated high risks, there has been efforts to model landslide susceptibility in the Himalayan regions based on currently available data with limited resolutions (Devkota et al., 2013; Regmi et al., 2014; Mandal & Mandal, 2018; Chowdhuri et al., 2021). Our work aims to capture the regional-scale, spatial distributions of landslide occurrences, differentiate controls of landslide hazards, and provide interpretable, essential empirical relationship between landslide controls and regional-scale landslide susceptibility. The decoupled, SNN identified functions combined with future changes in environmental conditions (e.g., extreme precipitation) may provide a promising tool for assessing the potential landslide hazards in this area (e.g., (Kirschbaum et al., 2020)). Our work is the first application XAI to landslide hazard, The method is easily applicable to other locations, different datasets, and other physical hazards, such as earthquakes and wildfires. The SNN is remarkably simple consisting of only two hidden layers yet its performance rivals that of DNNs. Our SNN can be also easily updated and improved when global, open-source, high-resolution datasets and high-performance computational resources become more available in the future.

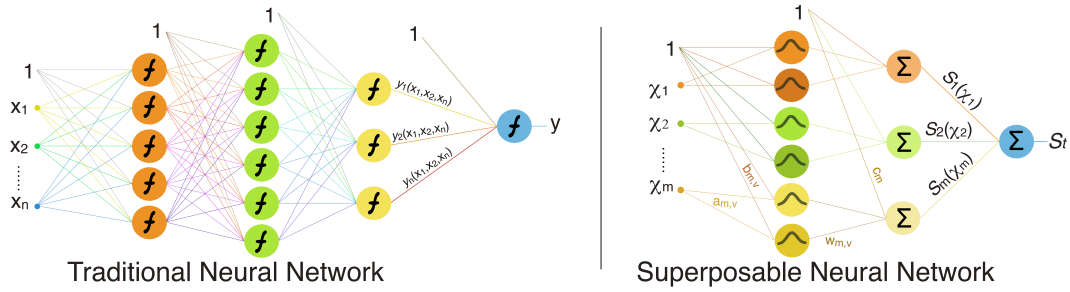


Figure 1. Conventional DNN architecture vs SNN architecture. In a conventional DNN, features are interconnected and interdependencies are embedded in the network, making them virtually impossible to separate. In a SNN, features and feature interdependencies that contribute to the output are found in advance and explicitly added as independent inputs. The symbols in this figure are defined in the main text, Equation 2. Details of the SNN architecture are explained in section 2.1.

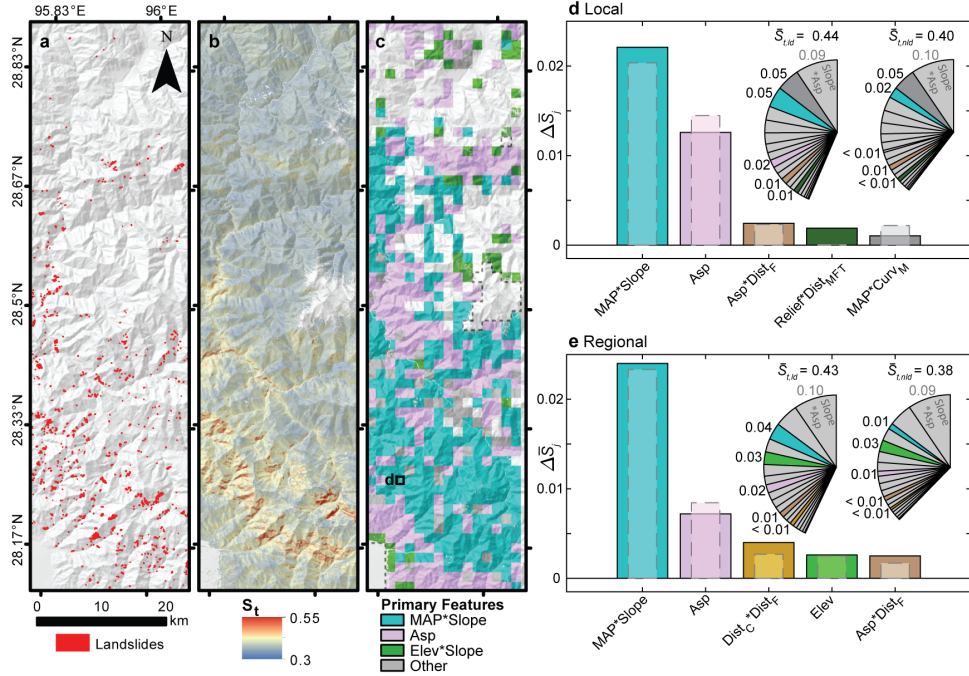


Figure 2. Spatial distribution of landslides, susceptibility, and important controls in the eastern end of Himalaya. Maps are shown for (a) 959 numbers of mapped landslides in red polygons, (b) total susceptibility at the pixel scale (S_t) from the Level-2 superposable neural network, and (c) primary features identified as locally important controls of landslides for the N-S region of the eastern end of Himalaya. A location of the region is shown in Fig. S2. The locally important control is identified as the feature with the largest difference in average contribution ($\Delta \bar{S}_j$) between areas of landslides (ld) and non-landslides (nld) within a 2.25 km² window. Windows of no data in (c) are due to the lack of landslide mapping, shown in gray dashed outlines, or modeled landslides. Bar charts represent $\Delta \bar{S}_j$ in descending order, and pie charts represent average S_j (\bar{S}_j) contributions to ld and nld areas for (d) an example of the local area shown with a white square in (c) and (e) the entire region. Bars with solid black and gray dashed borders show $\Delta \bar{S}_j$ based on modeled and manually mapped landslide inventories, respectively. Features related to topography, aspect, climate, and geology are shown in green, pink, blue, and brown or combinations thereof, respectively. Features outside of those are shown in gray. Mean annual precipitation (MAP), aspect (Asp), elevation ($Elev$), distances to channel ($Dist_C$), all faults ($Dist_F$), and main frontal fault and suture zone ($Dist_{MFT}$), and mean curvature ($Curv_M$). The asterisk * indicates algebraic multiplication of two features. Information regarding features and variables is provided in Supporting Information.

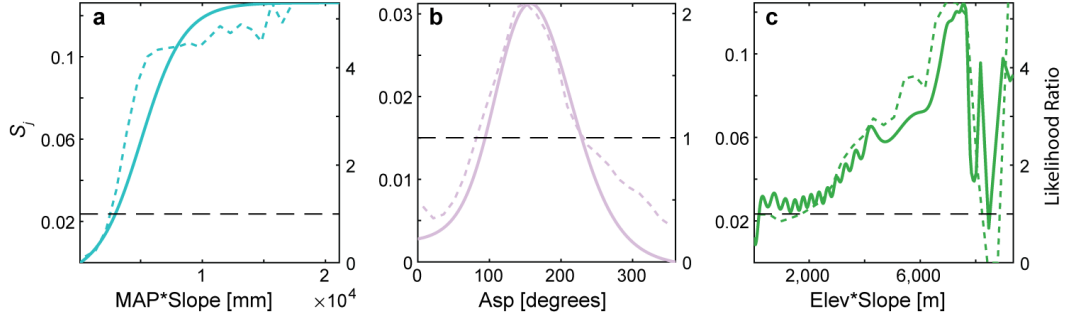


Figure 3. Feature contribution to susceptibility (S_j). Independent functions of S_j , identified as primary landslide controls for the N-S region, are shown for a) mean annual precipitation (MAP) * $Slope$, b) aspect (Asp), and c) elevation ($Elev$) * $Slope$. Likelihood ratios (LR) represent the likelihood of landslide occurrence for a specific range of feature values, which is calculated as the ratio of the probability of landslide occurrences to the probability of total area for the given feature range. $LR = 1$ and $LR > 1$ represent the average and above-average likelihood of landslide occurrence, respectively. LR are shown as short dashed lines with corresponding right-side y -axes. Note that S_j corresponding to $LR = 1$, shown as a long-dashed gray line, differ between features because the SNN quantifies the absolute contributions of S_j decoupled from other features. Colors are the same as those in Fig. 2c.

Open Research

For mapping landslides and quantifying landslide controls, we use publically available satellite data such as 30 m resolution Landsat 8 imagery, the 90 m digital elevation model from the Shuttle Radar Topography Mission (SRTM) (United States Geological Survey EarthExplorer, 2020), rainfall rates and variability from TRMM (Bookhagen & Burbank, 2010), and published geologic maps (Haproff et al., 2019; Taylor & Yin, 2009). The details of the models are provided in the Supporting Information.

Acknowledgments

L.-S.B. would like to thank NVIDIA for donating the Quadro P6000 GPU for this project. S.M. acknowledges the support of NSF EAR-1945431. We thank George Hilley, Dino Bellugi, Eitan Shelef, and Justin Higa for discussions and Ben Mirus for constructive review of an earlier version of the manuscript.

Supporting Information for “XAI Model for Accurate and Interpretable Landslide Susceptibility”

Contents

1. Text S1. SNN Training Method
2. Text S2. Description of Landslide Inventory
3. Text S3. Feature Descriptions and Limitations
4. Text S4. Explanations for the Controls on Landslide Occurrences
5. Text S5. Assessments of Model Performances
6. Text S6. Toy model
7. Table S1. Description of Landslide Inventory
8. Table S2. Description and Ranges of 15 Single Features
9. Table S3. Performance metrics for Models and Single Features
10. Table S4. Artificial Neural Network and Statistical Model Confidence Intervals
11. Table S5. Performance Metrics
12. Table S6. Correlation Metrics Between Features (R-value)
13. Table S7. Logistic Regression Control Coefficients
14. Table S8. Truth table.
15. Table S9. Composite features.
16. Figure S1. Superposable neural network training flow diagram.
17. Figure S2. Elevation map of the eastern end of Himalaya.
18. Figure S3. Spatial distribution of 15 features used in the SNN model.
19. Figure S4. Comparison between the feature ranges in three regions.
20. Figure S5. Spatial distribution of landslides, susceptibility, and important controls for the NW-SE region.
21. Figure S6. Spatial distribution of landslides, susceptibility, and important controls for the E-W region.
22. Figure S7. Bar charts representing $\Delta\bar{S}n_j$ from different methods.
23. Figure S8. Local analysis of climate vs slope susceptibility contributions to landslide occurrence .
24. Figure S9. Primary landslide controls for the NW-SE region are shown.
25. Figure S10. Primary landslide controls for the E-W region are shown.
26. Figure S11. The relationship among aspect, normalized difference vegetation index, and S_{Asp}
27. Figure S12. Feature ranking for Toy Model
28. Figure S13. Individual feature functions and target and SNN output for Toy Model.
29. Figure S14. Target and SNN output with noise for Toy Model.

S1 Text S1. SNN Training Method

Based on 15 single features, we modeled landslide susceptibility following the SNN architecture. Our SNN model allowed for the exploration of multiple combinations of parameters (e.g., 120 composite features for Level-2) without relying on an expert’s choices, precondition, or classification of input features. Our model found the most relevant features using a tournament ranking approach we designed to quantify each control’s contribution to susceptibility (S_j , where j corresponds to single or composite features) based on multiple steps of knowledge distillation. By superposing S_j , we produced the total landslide susceptibility map, S_t , a number ranging from 0 to 1 as the final product. Below are the details of SNN training method.

S1.1 Algorithm

The flow diagram of the superposable neural networks (SNN) training method is presented in Figure S1. The SNN is an additive model (Hooker, 2004; S. Tan et al., 2018) with a unique architecture described by eq. (2) and Fig. 1, and a unique training method explained here. Radial basis (Gaussian) activation functions are used, where each neuron is connected to one input only. The method consists of two main stages: feature-selection and knowledge distillation. A set of optimal composite features are identified in the feature selection stage, and multiple steps of knowledge distillation are used to create an SNN. The SNN inputs are composite features corresponding to a specific location, and the SNN output is the estimated landslide susceptibility (S_t) at that location. A validation of our approach using a toy model where we demonstrate the ability to extract boolean relationships from synthetic data is included in Supporting Information.

The method can be summarized by the following steps:

1. Multivariate polynomial expansion: composite features are generated.
2. Tournament ranking: an automated feature selection method we have designed for finding the features that are most relevant to the model.
3. Multistage training (MST): a second-order deep learning technique for generating a high-performance teacher network.
4. Fractional knowledge distillation: a technique we designed for separating the contribution of each feature to the final output.
5. Parallel knowledge distillation: standard knowledge distillation individually applied to networks corresponding to each feature.
6. Network superposition: merging single layer networks corresponding to each feature into one SNN.

These steps are explained in detail below.

S1.2 Multivariate polynomial expansion

Given n features x_1, x_2, \dots, x_n , we generate M composite features $\chi_1, \chi_2, \dots, \chi_M$ according to a predetermined maximum composite feature level.

Ex. 1: If the original number of features is 3 and the maximum composite feature level is Level-3, then we generate 13 composite features $[\chi_1, \chi_2, \dots, \chi_{13}] = [x_1, x_2, x_3, x_1 * x_2, x_1 * x_3, x_2 * x_3, x_1 * x_2 * x_3, x_1^2 * x_2, x_1^2 * x_3, x_2^2 * x_1, x_2^2 * x_3, x_3^2 * x_1, x_3^2 * x_2]$.

In this work, we have used 15 original features with a maximum composite feature Level-2. Because Level-3 performs marginally better than Level-2, we consider the Level-2 SNN as our optimal SNN. With 15 original features and the maximum

composite feature Level-2, we generate a total 120 composite features. All features are standardized with zero-mean and unit-variance.

S1.3 Tournament ranking

Our feature selection technique is based on a point system and uses a combination of backwards elimination and forward selection (L. Xu & Zhang, 2001) as building blocks. The composite features generated in the previous steps are randomly arranged into groups, with each group containing a subset of the features. Each feature group is used to train a simple neural network model. After the network is trained, backwards elimination is applied using area under the receiver operating characteristic curve (AUROC) as the performance criterion (Supporting Information). The top performing feature in the group receives a point. This process is repeated many times; several thousand groups were generated in the training of each SNN in this work. Features are ranked according to the points they accumulated. Forward selection is then applied in the order of the feature ranking to select the features that will be passed on to the next step.

The second-order Levenberg-Marquardt algorithm (Yu & Wilamowski, 2011) was used in training the individual neural networks models. It should be noted that using second-order training is essential for the practicality of this step. Unlike first-order training algorithms (based on gradient descent) that require manual hyper parameter tuning, second-order training algorithms are robust. In addition, second-order training can achieve better performance with fewer parameters (Ozyildirim & Kiran, 2020; Le et al., 2011; Battiti, 1992; H. Tan & Lim, 2019; Montavon et al., 2012; Yu & Wilamowski, 2011; Wilamowski & Yu, 2010). This allows the automation of the process, and reduces the memory requirements for training the networks, yielding a more efficient parallel implementation on multicore processors.

S1.4 Multistage training

The high-ranked features that are passed on from the previous step are used to train a high-performance DNN. We chose MST as our DNN model, since it has shown superior performance in similar applications (Youssef et al., 2015; Bouchard & Youssef, 2018; Youssef et al., 2018a).

S1.5 Fractional knowledge distillation

Knowledge distillation is a technique to reduce model complexity, by using the soft output of a more complex teacher DNN as the target of a less complex student DNN (Hinton et al., 2015). The MST in the previous step acts as our teacher network.

We have designed a variation of knowledge distillation that allows us to isolate the contribution of each feature to the estimated output. We call this variation *fractional knowledge distillation*, a term that is inspired by the fractional distillation technique in chemistry. We illustrate this using a step-by-step example for the case of two features. This can be easily generalized to any number of features.

Ex. 2: Assume that two composite features $[\chi_1, \chi_2]$ are passed on from the feature selection stage, and ordered according to importance where χ_1 is the most important. Let ts_0 be the set of soft targets obtained from the MST output:

1. Save a copy of ts_0 , named ts_{0c}
2. Train a simple DNN $net_{1,1}$ using only χ_1 as input and ts_0 as an output
3. Obtain $o_{1,1}$, the set of outputs of $net_{1,1}$
4. Update ts_0 to $ts_0 - o_{1,1}$

5. Train a simple DNN $net_{2,1}$ using only χ_2 as input and ts_0 as an output
6. Obtain $o_{2,1}$, the set of outputs of $net_{2,1}$
7. Update ts_0 to $ts_0 - o_{2,1}$
8. Evaluate performance by calculating AUROC using $\sum_{i=1}^2 \sum_{j=1}^1 o_{i,j}$ and ts_{0c}
9. Train a simple DNN $net_{1,2}$ using only χ_1 as input and ts_0 as an output
10. Obtain $o_{1,2}$, the set of outputs of $net_{1,2}$
11. Update ts_0 to $ts_0 - o_{1,2}$
12. Train a simple DNN $net_{2,2}$ using only χ_2 as input and ts_0 as an output
13. Obtain $o_{2,2}$, the set of outputs of $net_{2,2}$
14. Update ts_0 to $ts_0 - o_{2,2}$
15. Evaluate performance by calculating AUROC using $\sum_{i=1}^2 \sum_{j=2}^2 o_{i,j}$ and ts_{0c}
16. Repeat n times until the performance stops improving

Each DNN above consists of only a few neurons and is trained for a small number of epochs where the contribution of each feature is gradually determined to avoid numerical instabilities. The number of neurons and epochs are hyper parameters that can be tuned based on the data.

S1.6 Parallel knowledge distillation

The outputs from groups of networks, corresponding to each feature from the previous step, are added together to yield one soft target per feature. Knowledge distillation is separately used to train a single SNN layer for each feature.

Ex. 3: Following the previous example:

1. Create two soft targets: $ts_1 = \sum_{j=1}^n o_{1,j}$, and $ts_2 = \sum_{j=1}^n o_{2,j}$
2. Train a single layer network net_1 using χ_1 as input and ts_1 as an output
3. Train a single layer network net_2 using χ_2 as input and ts_2 as an output

S1.7 Network superposition

The single layer networks from the previous step are merged together to create the SNN, by adding an output layer that sums up the outputs of all the networks from the previous step. The connection weights at the output layer are set to one. The output of the SNN is a continuous value between 0 and 1, which determines the network’s estimation of landslide susceptibility at a specific location.

Ex. 4: Following the previous example, an SNN is created with χ_1 and χ_2 as inputs and $O = o_1 + o_2$ as the output, where o_1 is the output of net_1 and o_2 is the output of net_2 .

S1.8 Final notes

In this work, we have created three SNNs for three regions. The data samples from each region were partitioned into roughly 70% for training and 30% for testing. All reported results in the paper were obtained using the testing portion of the data.

Class imbalance was taken into consideration when training the networks. Given that the percentage of positive targets (locations containing a landslide) in each region is significantly smaller than negative targets (locations with no landslide), positive targets were weighted higher than negative targets in the training cost functions following the approach in (Youssef et al., 2018b).

S2 Text S2. Description of Landslide Inventory

The landslide inventory was obtained from manual mapping supplemented by an automatic detection technique. The basic procedure is as follows. We initially mapped landslides using Landsat 8 satellite imagery from November 12, 2017. We then used convolutional neural networks (CNN) to detect landslides automatically, according to (Ghorbanzadeh et al., 2019; Prakash et al., 2020). The CNN method used Landsat images and topographic and climatic attributes of mean curvature, elevation, local relief, mean annual precipitation, slope, failure index, and wetness to detect the landslides and test against the manually mapped landslides. We then manually corrected landslides from the automatic detection method using Landsat images, high-resolution satellite images from Google Earth, and a 4-band Planetscope Scene with a 3 m resolution. Manual correction is needed due to a common problem of inaccurately representing landslide areas because of aggregated features and small detected features that are not related to landslides in automatically mapped inventories (Marc & Hovius, 2015; Parker et al., 2011). We divided aggregated features into multiple landslides following suggestions from a previous study (Marc & Hovius, 2015). We used the manually corrected, automatically mapped landslides as our final landslide inventory (hereafter called semi-automated landslides).

Most landslides are a combination of source and deposit, which are difficult to distinguish in coarse resolution Landsat bands. Whenever possible, we excluded debris transport or deposits and only mapped landslide scars associated with source areas. In addition, we only assessed regions where landslides have the potential to occur or be detectable. Thus, areas of topographic slope less than 0.06 and alpine areas without vegetation cover were excluded from our landslide mapping and analysis. A slope threshold of 0.06 was determined to be the minimum slope along which landslides occur based on a cumulative distribution function of slope from observed landslides in the eastern end of Himalaya. The criteria based on terrain characteristics such as slope or local relief has been used in previous studies to constrain the area of the landslide analysis (Parker et al., 2011). Alpine areas were classified using spectral signatures representing snow cover in Landsat 8 imagery from February 2018. The areas excluded from our mapping are shown in gray dashed outlines in Fig. 2.

Our landslide inventory is comprised of semi-automated landslides includes 2,289 landslides covering a total area of 2.83×10^7 m², and a landslide density of 0.007 over a 4.19×10^9 m² mapped region (Table S1). Areas commissioned by semi-automatic detection but not manual mapping were ~ 0.1 , ~ 0.4 , $\sim 0.1\%$ of the total study area, while areas omitted by automated detection were ~ 0.2 , ~ 0.6 , $\sim 0.1\%$ of the total area.

The manually and semi-automatically detected landslides show a good correspondence ($>90\%$ match for landslides >4 pixels ($3,600$ m²) based on object identification that examine the existence of overlapping areas. Generally, most landslides missing from the manually detected inventory are objects with a small number of pixels that are not easily and objectively detected by humans. Semi-automated landslides with ≤ 4 pixels comprise $\sim 7.5\%$ of total landslide areas. When comparing these pixels with high-resolution Planetscope Scene satellite images during the post-processing procedure, we find that many of these pixels are indeed small landslides showing different spectral signatures. Thus, we include these semi-automatic landslides with ≤ 4 pixels in our final inventory. The area frequency distribution of our landslides from manual and semi-automatic mappings before 2017 shows a similar distribution to pre-2007 landslides from a nearby eastern Himalaya region that are manually mapped using 15-30 m resolution ASTER and Landsat images (Larsen et al., 2010; Larsen & Montgomery, 2012). Previous studies (Larsen et al., 2010; Larsen & Montgomery, 2012) used a landslide area of $100,000$ m² for the transition between soil and bedrock landslides in the nearby area. Considering that $<1\%$ of landslides in numbers and $<20\%$

of total landslide area are greater than 100,000 m², most of the landslides in our semi-automated inventory are likely soil landslides.

S3 Text S3. Feature Descriptions and Limitations

Here we explain how we obtained and calculated the 15 single features. The 15 single features include aspect (*Asp*), mean curvature (*Curv_M*), planform curvature, profile curvature, total curvature, discharge, distance to channel (*Dist_C*), distance to faults (*Dist_F*), distance to the Main Frontal Thrust and suture zone (*Dist_{MFT}*), drainage area, elevation (*Elev*), local relief (*Relief*), mean annual precipitation (*MAP*), number of extreme rainfall events (*NEE*) and slope. The inclusion of these variables is based on previous studies that examined the controls of landslides in the Himalayan regions (Devkota et al., 2013; Regmi et al., 2014; Mandal & Mandal, 2018; Chowdhuri et al., 2021).

First, topographic variables such as slope, aspect, local relief, curvature, distance to channel, and drainage area were calculated from a 90 m SRTM Digital Elevation Model (DEM) (United States Geological Survey EarthExplorer, 2020). Although a higher-resolution 30 m DEM is available, it contains missing values within our study area. Thus, we used a 90 m DEM for calculating topographic variables. Slope was calculated as the steepest descent gradient using an 8-direction (D8) flow routing method (Schwanghart & Scherler, 2014). We calculated aspect, the direction of slope face, as the angle in degrees clockwise from north given by the components of the 3-D surface normal. The surface normal was calculated using the *x*, *y*, and *z* components of each pixel. Local relief was calculated as the range in elevation within a 2.5 km radius circular window. We used a 2.5 km radius window because it is similar to the length scale of across-valley widths of channels in the range front where most landslides are. Local relief at this scale allows us to quantify the spatial variation of topographic relief relevant to landslides on these fluvial valleys. Curvature was calculated as the second derivative of the 90 m SRTM DEM. We calculated mean, planform, profile, and total curvatures using TopoToolbox 2 (Schwanghart & Scherler, 2014; Schmidt et al., 2003).

To calculate distance from channel, we first determined flow direction using D8 flow routing. The flow direction was carved through topographic depressions and flat areas to avoid sinks and generate a continuous drainage system. We then imposed a minimum drainage area of 1 km² needed to initiate stream before extracting a stream network based on the flow direction. Using the stream network, we calculated the distance of each pixel in the DEM to the nearest location in the stream network.

We acquired *MAP* and *NEE* from a previous study (Bookhagen & Burbank, 2010) that analyzed the Tropical Rainfall Measuring Mission (TRMM) 2B31 datasets from January 1998 to December 2009. Daily rainfall and *MAP* values were integrated from 3-hour measurements over 12 years. To calculate *NEE*, the 90th percentile of daily rainfall total for each pixel was determined for the 12-year measurement period (Bookhagen & Burbank, 2010). Only days with measured rainfall were included in calculating the probability density function. The number of days per year with daily rainfall total above the 90th percentile was counted as *NEE* (Bookhagen & Burbank, 2010; Bookhagen, 2010). The resolution of the original *MAP* and *NEE* datasets in our study area was ~ 2.6 km, which we resampled to 30 m resolution to be consistent with the resolution of our landslide inventory. To calculate the drainage area, we first calculated D8 flow directions of stream networks and calculated the number of upstream cells that contribute to each pixel. The number of cells can then be converted into a drainage area. Discharge was calculated by summing upstream contributing cells weighted by their *MAP* to account for spatially varying precipitation patterns. Using these weights, cells with higher *MAP* values will contribute more to total discharge than cells with lower precipitation values.

Previous studies (Parker et al., 2011; C. Xu et al., 2014) have shown that distance to fault ruptures is a good predictor for the occurrence of earthquake-induced landslides. We do not have information on active fault planes at depth and ground peak acceleration patterns for past earthquakes in these regions. Thus, we calculated $Dist_{MFT}$ for our study regions as each pixel’s Euclidean distance from the closest point on traces of the Main Frontal Thrust (MFT) and suture zones mapped by Taylor and Yin. (Taylor & Yin, 2009) These faults represent potentially active faults in our study area (Haproff et al., 2019, 2020). Because the suture zone is located far to the north, $Dist_{MFT}$ largely reflects the distance to the MFT. In addition, we calculated $Dist_F$ as the Euclidean distance of each pixel from boundaries separating all lithologic units reported in (Haproff et al., 2019). We include $Dist_F$ because bedrock tends to be more damaged near major lithologic boundaries due to faulting, which may influence landslide occurrences. The Euclidean distance was calculated using ArcGIS 10.6.

We note that there are limitations of our data from the eastern end of Himalaya. Landslide and input feature data have relatively coarse spatial resolutions and are based on limited spatial and temporal information (e.g., 30 m resolution Landsat satellite images from 2017 (United States Geological Survey EarthExplorer, 2020), 90 m resolution SRTM DEM (United States Geological Survey EarthExplorer, 2020), and ~ 2.6 km resolution TRMM data over 12 years (Bookhagen & Burbank, 2010)). We don’t have readily available high-resolution data on topography, surface materials (e.g., soil depth, bedrock structures, lithology), and climatic and ecohydrologic conditions (e.g., landslide-triggering storm intensity, time-series precipitation intensity, vegetation types). Though limited high-resolution satellite imagery is available (e.g., Planetscope Scene) in the area, we used relatively coarse 30 m resolution Landsat images because 1) Landsat images are globally available, open-source satellite images with a ~ 40 -year historic archive, 2) topographic, climatic, and geologic feature data have coarser resolutions than 30 m, and 3) we cover a large region of the eastern Himalaya (a total area of 4.19×10^9 m², 4.66×10^6 pixels at 30 m). For modeling a regional-scale study covering a large area, limited input data resolution, and computational costs, the use of 30 m resolution for our model was inevitable. Although our inventory is based on coarse 30 m resolution Landsat images, our inventory generated by semi-automatic mapping includes many small landslides missed by humans, but detected by an automatic detection algorithm based on a DNN and confirmed by high-resolution satellite images (see section S1). Thus, our landslide inventory captures the regional-scale, spatial distributions of landslide occurrences and provides essential information for regional-scale landslide susceptibility models. Due to the uncertainties in feature data, our landslide susceptibility model and feature analysis may also contain similar uncertainties and may change with updated, high resolution input data. However, our work presents more accurate and highly interpretable landslide susceptibility model based on currently available data, which can be readily available for hazard prediction and mitigation. Our SNN will be also easily applicable to other locations and different datasets when global, open-source, high-resolution datasets and high-performance computational resources become more available in the future.

S4 Text S4. Explanations for Landslide Controls

Here we explain how key results from the SNN can provide insights into the physical controls and mechanisms of landslides. A physically-derived metric, failure index (FI), based on limit equilibrium represents landslide propensity on an infinite slope for cohesionless material considering the pore pressure effect (Montgomery & Dietrich, 1994; Moon et al., 2011). This metric is similar to an inverse of factor of safety and can be related to total landslide susceptibility (S_t). We can formulate FI

as:

$$FI = \frac{S}{S_0} \left(1 - W \frac{\rho_w}{\rho_s} \right)^{-1} \quad (2)$$

where S_0 is the threshold slope, S is the local slope, ρ_s is the wet bulk density of soil (2.0 g/cm³), ρ_w is the bulk density of water (1.0 g/cm³), and W is wetness that represents the degree of subsurface saturation. W varies from 0 (unsaturated) to 1 (fully saturated). This equation can be further expanded by Taylor series:

$$FI \approx \frac{S}{S_0} \left(1 + W \frac{\rho_w}{\rho_s} + W^2 \left(\frac{\rho_w}{\rho_s} \right)^2 + O(W^3) \right) = \frac{S}{S_0} (k(W)). \quad (3)$$

The approximated FI has three components, local slope S , threshold slope S_0 , and $k(W)$ that represents the degrees at which landslides are promoted by subsurface saturation. $k(W)$ varies from 1 (unsaturated) to 2 (fully saturated).

A change in climatic conditions can increase volumetric water content and pore-water pressure and lead to an increased degree of subsurface saturation (i.e., W) and subsequently induce slope failure. Previous physically-based slope stability models consider various climatic factors (e.g., rainfall amount and intensity, subsurface convergence flow) to deduce the degree of subsurface saturation to model rainfall-induced landslide occurrences (Montgomery & Dietrich, 1994; Baum et al., 2002, 2010). For example, the Shallow Landslide Stability model (SHALSTAB) (Montgomery & Dietrich, 1994; Dietrich et al., 2001) uses the topographic wetness index, proposed by Beven and Kirkby (1979) (Beven & Kirkby, 1979), to calculate subsurface saturation considering the convergence of shallow subsurface flow from up-slope drainage areas for a given steady-state precipitation. On the other hand, the Transient Rainfall Infiltration and Grid based Regional Slope stability model (TRIGRS) (Baum et al., 2002, 2010) calculates transient pore pressure development due to vertical rainfall infiltration from rainfall intensity.

In reality, both subsurface convergence and rainfall infiltration are essential contributors to subsurface saturation and need to be implemented in physically-based slope stability models. However, measuring precipitation intensity, moisture availability, or subsurface convergence and saturation is difficult, especially in rural mountainous areas with limited accessibility. Thus, the identification and quantification of various climatic contributions that promote landslides is challenging.

According to the Level-2 SNN model results, the most important, differentiating features for landslides in this area are the product of slope and mean annual precipitation (MAP) (N-S region) or the product of slope and number of extreme events (NEE) (NW-SE and E-W regions). This result implies that local precipitation infiltration influenced by precipitation rate and intensity, represented by MAP and NEE , may serve as a first-order control on $k(W)$ in equation 2. The absence of drainage area or discharge as a contributing feature to susceptibility may suggest that subsurface flow convergence may be a second order contributor to the landslides in the eastern end of Himalaya. However, we cannot rule out the possibility that the importance of topographic convergence was masked due to the low-resolution of input topographic and rainfall data, e.g. (Leonarduzzi et al., 2021). These factors can be further examined in future studies using high-resolution topographic and climate data.

In addition, the SNN identified aspect, the direction of slope face, as another primary feature that influences landslide occurrences. Previous studies considered slope aspect preference in terms of: 1) vegetation activity that affects root cohesion (McGuire et al., 2016), or 2) the orientation of wind-driven rainfall. To examine vegetation activity across hillslope aspect, we calculated the normalized difference vegetation index ($NDVI$) following the USGS procedure (Zanter, 2016). We first converted Landsat 8 Level-1 Digital Numbers to top-of-atmosphere (TOA) reflectance.

TOA reflectance eliminates the impact of different solar angles and illumination geometries and is calculated as:

$$\rho\lambda = \frac{M_\lambda Q_{cal} + A\rho}{\cos(\theta_{SZ})}, \quad (4)$$

where $\rho\lambda$ is the TOA reflectance, M_λ is the band-specific multiplicative rescaling factor from the Landsat 8 metadata, Q_{cal} is the standard product pixel values, $A\rho$ is the band-specific additive rescaling factor from the metadata, and θ_{SZ} is the local solar zenith angle.

We use the corrected bands 4 and 5 from Landsat 8 to calculate NDVI as:

$$NDVI = \frac{\text{band 5} - \text{band 4}}{\text{band 5} + \text{band 4}}, \quad (5)$$

where bands 4 and 5 represent the visible and near-infrared light reflected by vegetation, respectively. Healthy vegetation with high photosynthetic capacity absorbs a larger proportion of incident visible light while reflecting a greater portion of near-infrared light compared to sparse or unhealthy vegetation (Tucker et al., 1986). Therefore, an *NDVI* value close to 1 suggests a higher density of healthy vegetation and green leaves while a value near 0 might indicate unhealthy or no vegetation. We utilized Landsat 8 satellite imagery from October 2015, November 2017, and February 2018 (United States Geological Survey EarthExplorer, 2020) for our analyses of *NDVI*. These months were selected to characterize *NDVI* values before and after the summer monsoon season, during which a large proportion of landslides are suspected to occur because of intense rainfall. We excluded summer months from our analyses because of the abundant cloud cover present in those images, which masks the visibility of the land surface.

NDVI plotted against aspect in our study area shows a broad distribution of high values centered around values corresponding to south-facing slopes. However, this *NDVI* distribution is different from the observed peak of S_{Asp} around 145° to 180° (Figure S11). This result may imply that more landslides on south-facing slopes are likely due to orographic precipitation patterns caused by moisture delivery from the south rather than through the effects of vegetation. Previous work has characterized the northward moisture transfer to this study area from the Bay of Bengal during monsoon seasons (Bookhagen & Burbank, 2010; Barros et al., 2004; Yang et al., 2018). Thus, we think that the SNN-identified primary feature of aspect supports the influence of aspect-related differences in microclimate (e.g., moisture availability) on landslide occurrences in this area.

S5 Text S5. Assessments of Model Performances

We evaluate the performance of the SNN compared to traditional approaches using several performance metrics, including the area under the receiver operating characteristic curve (AUROC), the area under the success rate curve (AUC of success rate), accuracy, sensitivity (i.e., probability of detection, POD), specificity (i.e., probability of false detection, POFD), and POD-POFD following the literature. See, for example (Prakash et al., 2020). AUROC and AUC of success rate are cutoff-independent performance criteria while accuracy, POD, and POFD are cutoff-dependent. The AUROC is calculated as the area under a curve created by plotting the true positive rate against the false positive rate at various thresholds along a feature’s range. The AUC of success rate is calculated by plotting the fraction of landslide area correctly identified against the fraction of total area classified as positive (i.e., predicted landslides). AUC ranges between 0 and 1, with 1 indicating a perfect classifier and 0.5 indicating a random model. After generating a threshold-modeled landslide map based within the 30% testing partition using the optimal threshold corresponding to the point closest

to [0,1] on an AUROC curve, accuracy is calculated as the fraction of landslide and non-landslide area correctly classified by the model relative to all studied areas. POD and POFD measure the proportion of landslide areas correctly classified relative to all observed landslide areas and the proportion of incorrectly classified landslide areas relative to all observed non-landslide areas, respectively.

We calculate these metrics for all 15 single original features, a physically-based slope stability model (SHALSTAB), two statistical methods (logistic regression and likelihood ratios), a first-order artificial neural network (ANN) based on the adaptive moment estimation (Adam) optimization algorithm, and Level-1 and Level-2 SNNs.

First, we investigated each of the 15 single features as individual classifiers for landslide occurrences (Table S3). Second, we assessed the propensity of landslides using a topographic metric called the failure index. The failure index (FI) is the ratio of driving to resisting force on a hillslope, which is the inverse of the factor-of-safety. FI is modified from the SHALSTAB model that couples infinite slope stability and steady-state hydrology for cohesionless material (Montgomery & Dietrich, 1994; Dietrich et al., 1995, 2001; Moon et al., 2011). Considering that landslides smaller than 100,000 m² (the upper bound for soil landslides in this region (Larsen et al., 2010; Larsen & Montgomery, 2012)) constitute >99% of landslides in number and ~80% of total landslide area, we assume that most landslides in our inventory are soil landslides.

To calculate the FI , we first determine the spatial distribution of wetness (W), which represents the degree of subsurface saturation. W is calculated as a ratio between local hydraulic flux from a given steady-state precipitation relative to that of soil profile saturation (Montgomery & Dietrich, 1994):

$$W = \frac{h}{z} = \frac{qA}{bT \sin \theta} \quad (6)$$

where h is the saturated height of the soil column (L), z is the total height of the soil column (L), q is the steady-state precipitation during a storm event (L/T), A is the drainage area (L^2) draining across the contour length b (L), T is the soil transmissivity when saturated (L^2/T), and θ is the local slope in degrees. W varies from 0 (unsaturated) to a capped value of 1 (fully saturated). We used a base value of 1×10^{-4} m²/s for T following Moon et al. (Moon et al., 2011) We used the spatial distribution of MAP (Bookhagen & Burbank, 2010) to represent the steady-state precipitation, q . We then calculated the spatial distribution of FI as:

$$FI = \frac{S}{S_0} \left(1 - W \frac{\rho_w}{\rho_s} \right)^{-1} \quad (7)$$

where S_0 is the threshold slope set at 45°, S is the local slope, ρ_s is the wet bulk density of soil (2.0 g/cm³), and ρ_w is the bulk density of water (1.0 g/cm³). To examine whether the model performance of FI is different when predicting all landslides vs soil landslides, we include the results of the performance metrics for FI calculated using all landslides and soil landslides in Table S3.

Third, we applied two statistical models, logistic regression and likelihood ratios, to assess landslide susceptibility. Logistic regression (hereafter, LogR) is based on a multivariate regression between a binary response of landslide occurrence and a set of predicting features that are continuous, discrete, or a combination of both types (Lee, 2005). To build these models, we consider only one curvature metric following Lee (Lee, 2005), instead of using all four different curvatures. We selected $Curv_M$ to build the statistical models. In addition, we consider $\log_{10}(\text{drainage area})$ and $\log_{10}(\text{discharge})$ because of their inverse power-law relationships with landslide and debris flow incision (Stock & Dietrich, 2003, 2006). The relationship between features and landslide

occurrence can be displayed as:

$$p = \frac{e^c}{e^c + 1} \quad (8)$$

where p is the probability of landslide occurrence that varies from 0 to 1 in an S-shaped curve, and c is the linear combination of features:

$$c = b_0 + b_1x_1 + b_2x_2 + \dots + b_nx_n \quad (9)$$

where x_i ($i = 1, 2, \dots, n$) represents each feature, b_i represents the optimized coefficient, and b_0 represents the intercept of the model. Utilizing Eqs. 8 and 12, we obtain an extended expression for the LogR model relating the probability of landslide occurrence p and multiple features:

$$\text{logit}(p) = \log\left(\frac{p}{1-p}\right) = b_0 + b_1x_1 + b_2x_2 + \dots + b_nx_n \quad (10)$$

where \log is the natural log. To determine any possible collinearity between features, we calculate the correlation coefficient (R) between all combinations of 12 features (Table S6). We observed maximum absolute values of $R = -0.828$ (N-S), 0.717 (NW-SE), and 0.857 (E-W), which are below the threshold of 0.894 corresponding to a variance inflation factor of <5 , indicating low collinearity between features (Stine, 1995; Kavzoglu et al., 2014) and thus we used all 12 features. We treated aspect as a discrete feature due to its nonlinear relation with landslide occurrences. The best-fit coefficient values are shown in Table S7.

Similar to the SNN, the LogR method provides information on the importance of variables through the best-fit coefficients. To compare those results, we determined top features that differentiate areas with and without threshold modeled landslides based on the LogR output following similar procedures that we used for the SNN. The output of LogR ranges between 1.06×10^{-6} to 0.820 for the N-S region. The threshold value (t) of 0.005 that corresponds to the point closest to $[0,1]$ on an ROC curve (i.e., a perfect classifier) was used to classify landslide (ls) and non-landslide areas (nls) for the N-S region. We calculated $\Delta\bar{c}n_i$ as the difference between the average value of a feature multiplied by its respective coefficient for ls and nls areas, then divided by an adjusted threshold that was transformed from t (i.e., 0.005) from the LogR output according to the equation below:

$$\Delta\bar{c}n_i = \frac{\bar{c}_{i,ls} - \bar{c}_{i,nls}}{t_a} \quad \text{where } t_a = \log\left(\frac{t}{1-t}\right) - b_0, \quad (11)$$

where $\bar{c}_{i,a}$ is the average feature i value multiplied by its respective coefficient for areas (a) of ls or nls , and t_a is the adjusted threshold value based on b_0 , the overall intercept value determined by the LogR model, and t , the threshold determined using the ROC curve (i.e., 0.005 for the N-S region). We transformed t to t_a and used it for normalization to enable the direct comparison of results between LogR and SNN. For the SNN-determined primary features, we calculate $\Delta\bar{S}n_j$ as $\Delta\bar{S}_j$ divided by the threshold that classify landslides (i.e., 0.406 for the N-S regions). The value of 1 in both $\bar{S}n$ and $\bar{c}n$ represent the threshold susceptibility that classifies ls and nls areas. The results of the identified primary controls of landslides that induce large differences in average susceptibility between landslide and non-landslide areas in the N-S regions from LogR, SNN Level-1, and SNN Level-2 are shown in Figure S7. All methods identified climate-related factors (e.g., MAP, NEE, Asp) as primary controls; however, only SNN Level-2 was able to identify the importance of the composite feature *MAP*Slope*.

The likelihood ratio method uses the relationship between observed landslide occurrences and controlling feature ranges. Previous studies have quantified the ratio

of the probability of landslide occurrences to the probability of non-occurrences or all-occurrences and referred to it as the likelihood ratio, frequency ratio, or probability ratio (Lee, 2005; Akgun, 2012; Reichenbach et al., 2018). In this study, we calculate likelihood ratios (LR) as the ratio of the percentage of landslide pixels relative to total landslide pixels divided by the percentage of pixels relative to the total area for the specific range of feature values (Lee, 2005; Akgun, 2012). Landslide susceptibility for each pixel is calculated as the sum of the corresponding LR from each feature’s value. A ratio of 1 and >1 indicates the average and above-average likelihood of landslide occurrence within the feature range compared to that of the study area. Conversely, values less than 1 indicate a below-average likelihood. In this study, we used all 15 features with each feature’s range divided into ten bins to calculate LR and landslide susceptibility. The first and last bins represent areas less than and greater than the 10th and 90th percentile of LR , respectively, with values between these bins split into eight equal bin ranges.

Lastly, we applied a landslide susceptibility model based on an ANN using the Adam optimizer. We prepared landslide feature datasets following (Tien Bui et al., 2012). All features, except for planform, profile, and total curvatures, used to build the SNN were used to apply the Adam optimizer. We divided each of the 12 feature maps into 10 categories representing intervals for every 10th percentile. Then, we gave each category a normalized category value using the following Max-Min normalization formula: (Fernandes & Lona, 2005)

$$v' = \frac{v - \min(v)}{\max(v) - \min(v)}(U - L) + L \quad (12)$$

where v' is the normalized category value, v is the attribute value, and U and L are the upper and lower normalization range boundaries set as 0.1 to 0.9. Landslide inventories and feature maps were then partitioned into training (70%) and testing (30%) regions using the same checkerboard pattern applied when building the SNN.

The ANN analysis utilized 12 feature inputs and one network output. The structure was composed of an input layer, three fully connected layers with 200, 200, and 2 neurons per layer respectively, a softmax layer, and a classification output layer. The mini-batch size used for each training iteration was set to 64. The maximum number of epochs was set to 200. The initial learning rate was set to 2×10^{-4} . We used a piecewise method for learning rate with the default learning rate drop factor of 0.1 that is applied to the global learning rate every five epochs passed. The training data was shuffled before every training epoch. An early stoppage of 10 epochs without improvement in validation error was used to prevent over-fitting.

We determined a 95% confidence intervals of mean AUROC by conducting a 10-fold cross validation for all statistical and neural network models utilized in this study. We randomly and uniformly selected 50% of the original training pixels from the checkerboard pattern partition and trained the model on this portion of the training dataset. Subsequently, we tested the trained model on 50% of the testing dataset that was also selected randomly and uniformly. We then calculated the AUROC for each trial. This procedure was then repeated 10 times for each method and the results were used to calculate the 95% confidence interval for the mean AUROC and 2σ range of AUROC from 10 validation tests (Table S5).

Our model assessments for single features indicate that MAP [AUROC = 0.756 (N-S region)] and slope [AUROC = 0.696 (NW-SE), 0.760 (E-W)] are the highest performing single features. The SNN produces a 19-26% improvement in AUROC compared to a physically-based landslide model (e.g., failure index for all landslides or soil landslides). Additionally, the SNN produced up to ~8%, ~10%, and ~12% increases in performance compared to the logistic regression, likelihood ratio methods, and ANN-based susceptibility model, respectively. The physically-based model of FI

produces slightly different AUROC for predicting all landslides vs. soil landslides, but both AUROC values were lower than that of the SNN (Table S3). Further investigation using performance metrics including the AUC of the ROC, success rate, accuracy, POD, POFD, and POD-POFD reveals that the SNN outperformed the tested ANN, and statistical and physical models across all metrics (Table S4).

Although both likelihood ratios and the SNN reveal functional relationships between susceptibility and features, the SNN is more useful for landslide susceptibility assessment because it decouples individual feature contributions and quantifies absolute contributions from features and feature interdependencies. The SNN reveals the importance of features coupling slope and climatic factors (e.g., MAP^*slope , NEE^*slope) as a primary driver for landslide occurrence. Accounting for these under-appreciated features and feature interdependencies that are not generally implemented in statistical methods or physically-based models can lead to a substantial increase in performance.

S6 Text S6. Toy Model

There can be many solutions of models that can fit a dataset generated by another model with varying degrees of accuracy. In order to test whether our method can find a solution that closely matches a known existing model, consider the following constrained toy application by generating a dataset that represents a logical relationship and testing the behavior of our algorithm.

Take the equation

$$y = x1 * x2 + x3 * x4 - 2 * x1 * x2 * x3 * x4, \quad (13)$$

where $x1, x2, x3$ and $x4$ are Boolean values. It is easy to check that the equation represents the logical relationship

$$y = (x1 \wedge x2) \vee (x3 \wedge x4) \wedge \overline{(x1 \wedge x2 \wedge x3 \wedge x4)}$$

where the truth table is shown in Table S8.

We generated 1,000 random realizations of $x1_n, x2_n, x3_n$ and $x4_n$ and we calculate the corresponding value y_n for each of these realizations, where $n = 1 : 1000$. We tested our algorithm by training an SNN using $x1_n, x2_n, x3_n$ and $x4_n$ as the input and y_n as the target output, so as to test whether our method can infer the logical relationship from the basic components using only the generated data samples. Up to Level-4 composite features were used in this analysis, for a total number of 15 features as shown in Table S9.

The resulting feature ranking (Figure S12) shows that our algorithm was able to successfully isolate the composite features that exist in the relationship. The truth table (Table S8) reveals that the higher ranking given to $\{x1 * x2 * x3 * x4\}$ corresponds to the fact that this feature can decisively explain 50% of the logical relationship independently from the other features. If $\{x1 * x2 * x3 * x4\}$ is one, then y is always zero. On the other hand, the other features cannot decisively determine any part of the outcome on their own, but they can decisively determine the outcome if they depend on $\{x1 * x2 * x3 * x4\}$.

Our method was able to find a solution to the logical relationship that accurately matches the target output (Figure S13). Our model is given by

$$\tilde{y} = f(x1 * x2) + f(x3 * x4) + f(x1 * x2 * x3 * x4),$$

where

$$f(x1 * x2) \approx \begin{cases} 0.1, & \text{for } x1 * x2 = 0 \\ 1.1, & \text{for } x1 * x2 = 1 \end{cases}$$

$$f(x_3 * x_4) \approx \begin{cases} -0.25, & \text{for } x_3 * x_4 = 0 \\ 0.75, & \text{for } x_3 * x_4 = 1 \end{cases}$$

$$f(x_1 * x_2 * x_3 * x_4) \approx \begin{cases} 0.15, & \text{for } x_1 * x_2 * x_3 * x_4 = 0 \\ -1.85, & \text{for } x_1 * x_2 * x_3 * x_4 = 1 \end{cases}$$

Note that subtracting the two ends of the function of each feature returns the coefficient values in the original equation (Eq. 13) for each corresponding variable:

$$f(x_1 * x_2) : 1.1 - 0.1 = 1,$$

$$f(x_3 * x_4) : 0.75 - (-0.25) = 1,$$

$$f(x_1 * x_2 * x_3 * x_4) : -1.85 - 0.15 = -2.$$

Furthermore, the behavior of our method proved to be robust to noise. Figure S14 demonstrates the results of the same experiment, only this time the data was contaminated by adding Gaussian noise to $x_{1_n}, x_{2_n}, x_{3_n}$ and x_{4_n} prior to training and testing. Although the SNN output became noisier, the noise effect can easily be removed with thresholding and does not affect the outcome.

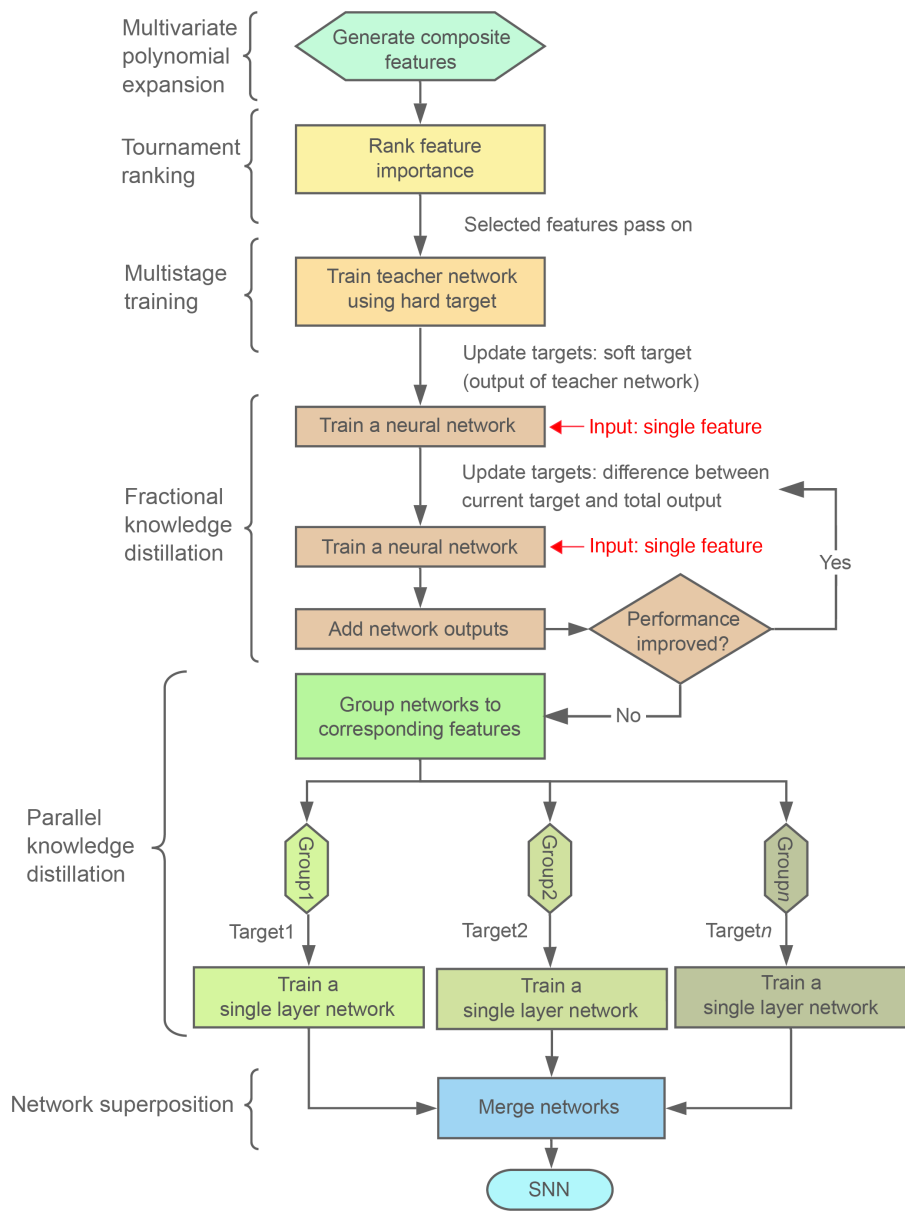


Fig. S1. Superposable neural network training flow diagram. The details of methodology are explained in the Data & Methods section (main text).

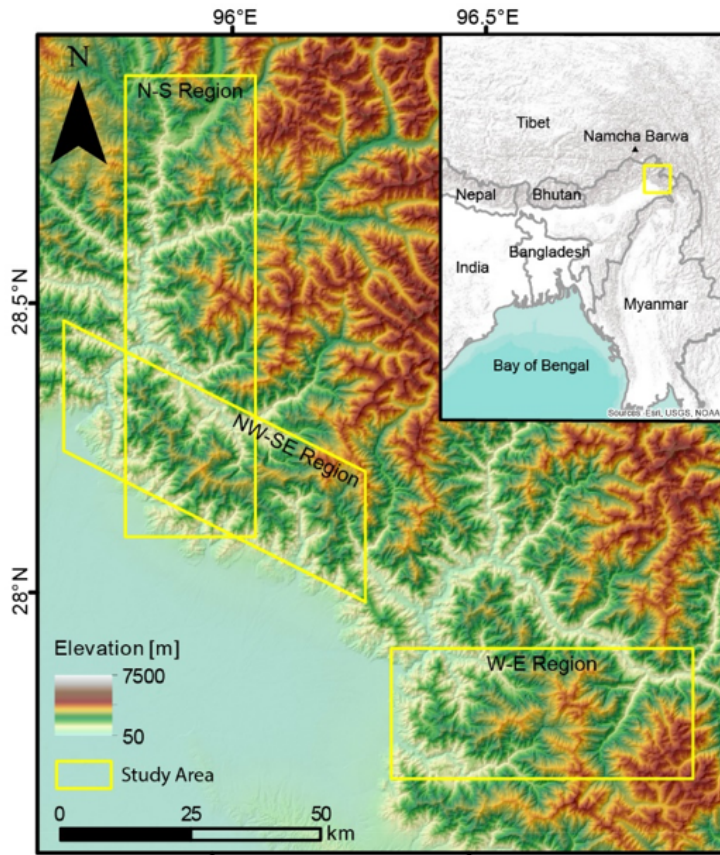


Fig. S2. Elevation map of the eastern end of Himalaya. Yellow boxes indicate our three N-S, NW-SE, and E-W oriented study regions. The inset map shows the Himalayan region with our study area shown in a yellow box and national borders shown with dark gray lines.

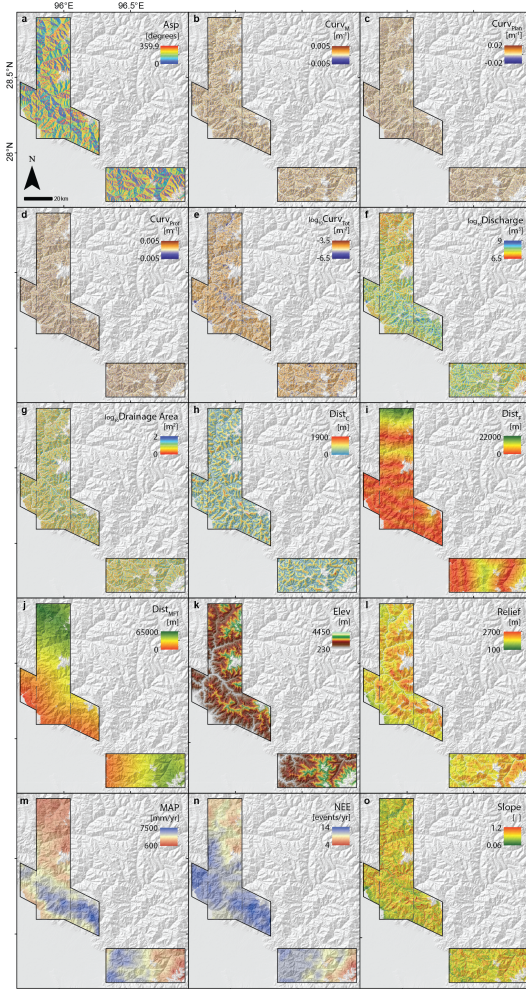


Fig. S3. Spatial distribution of 15 features used in the superposable neural network model. The 15 single features include (a) aspect (Asp), (b) mean curvature ($Curv_M$), (c) planform curvature ($Curv_{Plan}$), (d) profile curvature ($Curv_{Prof}$), (e) total curvature ($Curv_{Tot}$), (f) discharge, (g) drainage area, (h) distance to channel ($Dist_C$), (i) distance to faults ($Dist_F$), (j) distance to the Main Frontal Thrust and suture zone ($Dist_{MFT}$), (k) elevation ($Elev$), (l) local relief ($Relief$), (m) mean annual precipitation (MAP), (n) number of extreme events (NEE), and (o) slope. Dashed lines mark the overlapping area between the N-S and NW-SE region. Features in (e, f, g) are displayed on logarithmic scales.

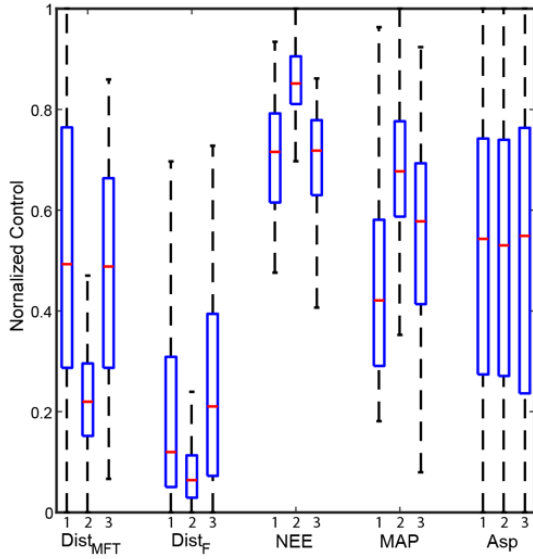


Fig. S4. Comparison between the feature ranges of distance to main faults ($Dist_{MFT}$), distance to faults ($Dist_F$), number of extreme rainfall events (NEE), mean annual precipitation (MAP), and aspect (Asp), each normalized by the maximum feature value across all three regions. Red center lines represent the median and top and bottom ends of the box represent the 25th and 75th quartiles, respectively. The ends of the dashed lines extending from each side of the box plot represent 1.5 times the interquartile range or the minimum or maximum values. Outliers are not shown in this figure. On the x -axis, 1, 2, and 3 correspond to the N-S, NW-SE, and E-W regions, respectively.

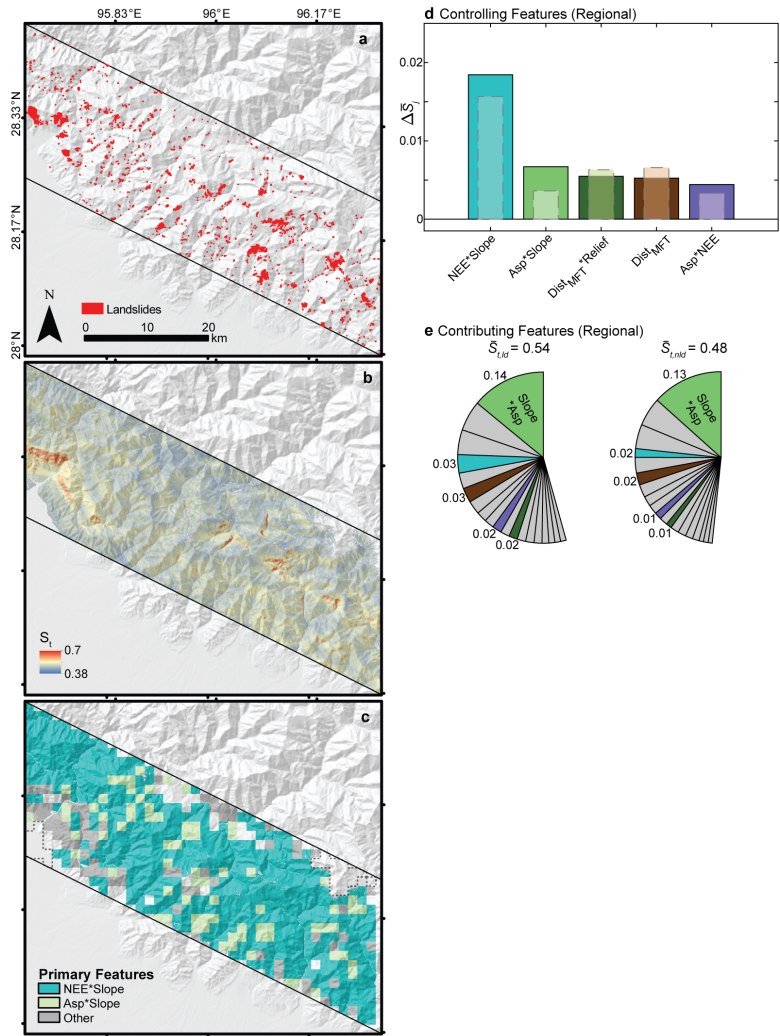


Fig. S5. Spatial distribution of landslides, susceptibility, and important controls for the NW-SE region. Maps are shown for (a) manually mapped landslides in red polygons, (b) total susceptibility (S_t) from the Level-2 superposable neural network, and (c) primary features identified as locally important controls of landslides. Bar charts in (d) represent $\Delta \bar{S}_j$ in descending order, and pie charts in (e) represent average S_j (\bar{S}_j) contributions to *ld* and *nld* areas for the entire region. Details are the same as in Figure 2.

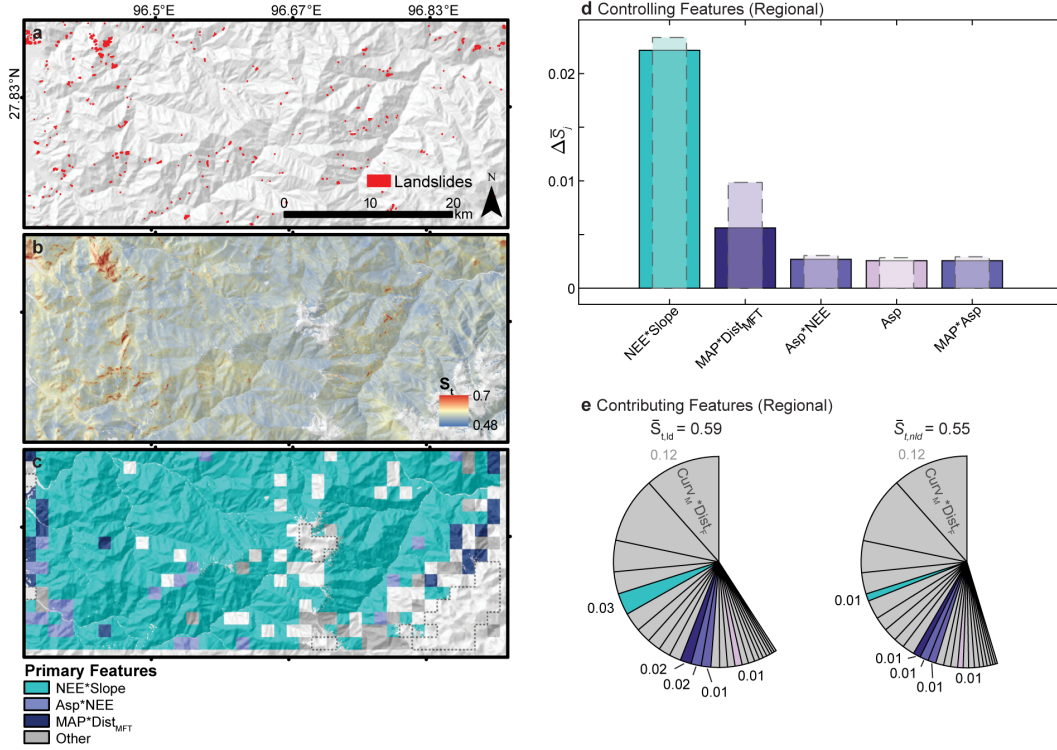


Fig. S6. Spatial distribution of landslides, susceptibility, and important controls for the E-W region. Maps are shown for (a) manually mapped landslides in red polygons, (b) total susceptibility (S_t) from the Level-2 superposable neural network, and (c) primary features identified as locally important controls of landslides. Bar charts in (d) represent $\Delta\bar{S}_j$ in descending order, and pie charts in (e) represent average S_j (\bar{S}_j) contributions to *ld* and *nld* areas for the entire region. Details are the same as in Figure 2.

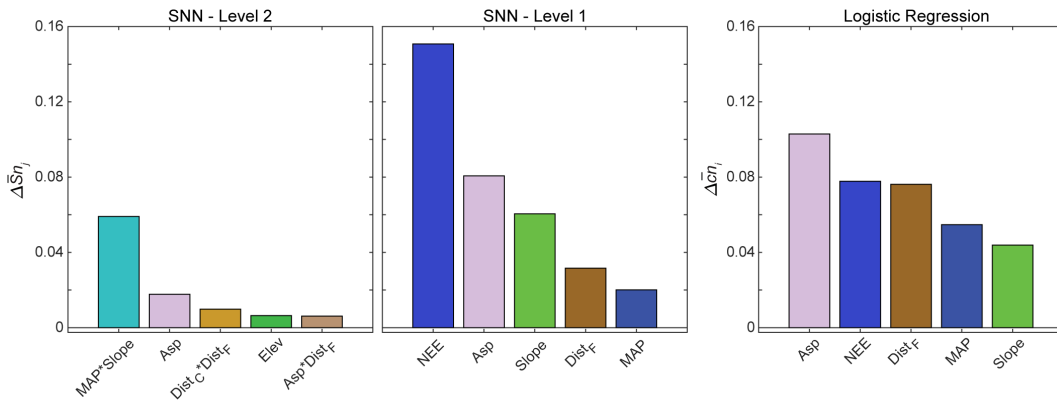


Fig. S7. Bar charts representing $\Delta\bar{S}_{n_j}$ for the (a) SNN - Level 2 and (b) SNN- Level 1 and $\Delta\bar{c}_{n_i}$ for (c) logistic regression, arranged in descending order. Details on the calculations of $\Delta\bar{S}_{n_j}$ and $\Delta\bar{c}_{n_i}$ are provided in the Supporting Information, page 24. Features related to topography, aspect, climate, and geology are shown in green, pink, blue, and brown or combinations thereof, respectively.

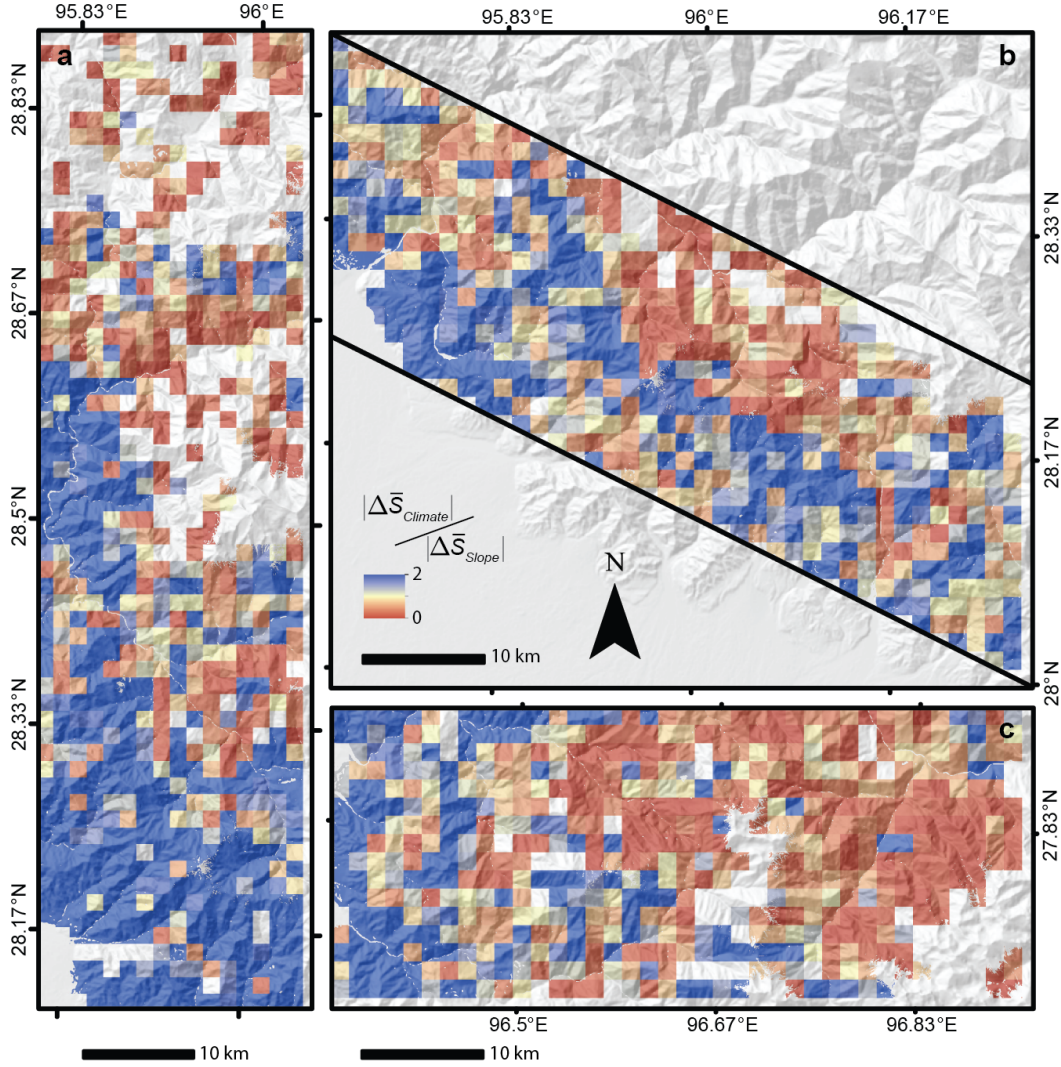


Fig. S8. Local analysis of climate vs slope susceptibility contributions to landslide occurrence for the (a) N-S, (b) NW-SE, and (c) E-W study regions. Values greater than 1 indicate a larger contribution from climate features ($\Sigma \Delta \bar{S}_{climate, j = Asp, NEE, MAP}$) relative to that of slope ($\Delta \bar{S}_{Slope}$). Windows of no data are due to no modeled or mapped landslides.

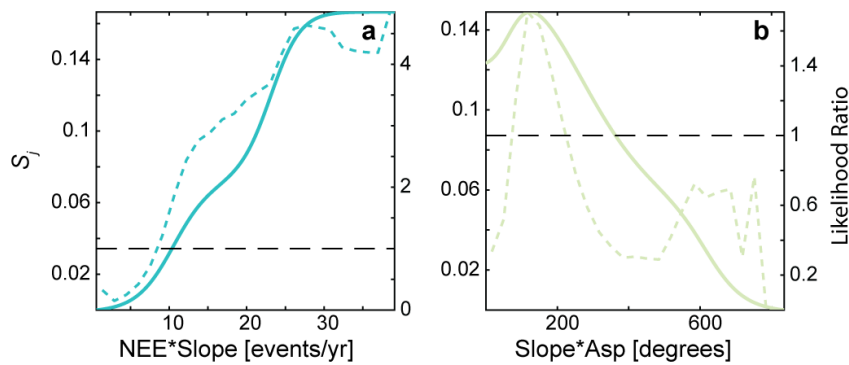


Fig. S9. Primary landslide controls of a) number of extreme events (NEE) * slope, and b) slope * aspect (Asp) for the NW-SE region are shown. Details are the same as in Figure 3.

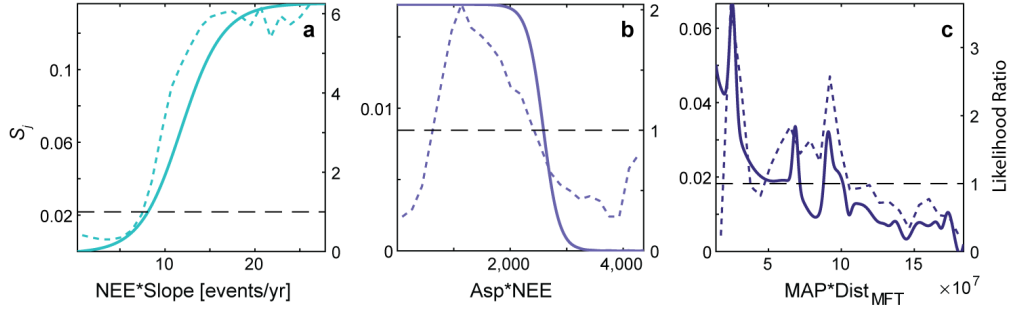


Fig. S10. Primary landslide controls of a) number of extreme events (NEE) * slope, b) aspect (Asp) * NEE , and c) mean annual precipitation (MAP) * distance to main faults ($Dist_{MFT}$) for the E-W region are shown. Details are the same as in Figure 3.

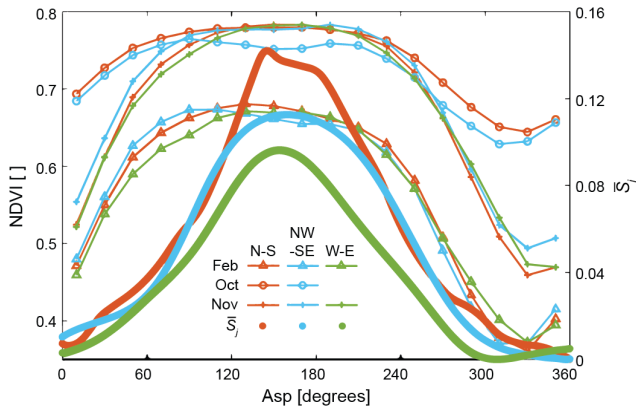


Fig. S11. The relationship between aspect and normalized difference vegetation index ($NDVI$), shown as thin lines, and S_{Asp} from SNN level-1, shown as thick lines. Colors correspond to different regions while symbols shown as thin lines correspond to different times of measurements (October 2015, November 2017, and February 2018). Symbols on thin lines represent the averaged $NDVI$ value for a 20° interval of aspect.

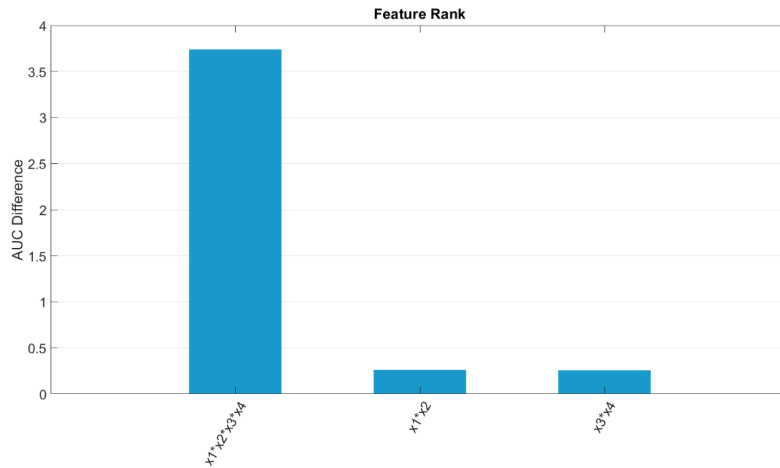


Fig. S12. Feature ranking.

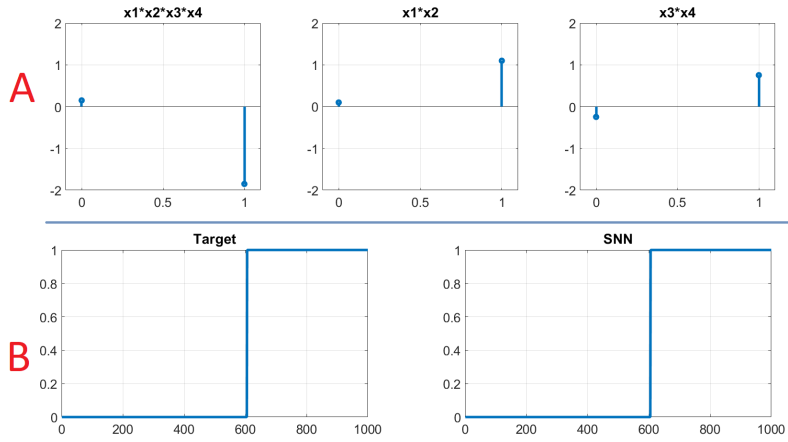


Fig. S13. (A) individual feature functions. (B) Target output v.s. SNN output.

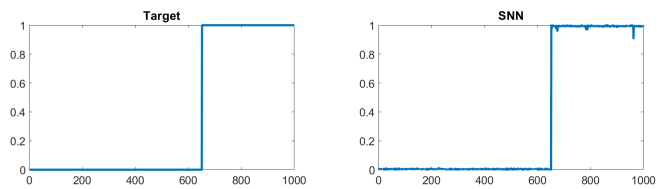


Fig. S14. Target output vs SNN output when data is contaminated with noise.

Supplementary Table S1. Description of Landslide Inventory

Table S1. Descriptor

	N-S		NW-SE		E-W		Overall	
	Auto	Manual	Auto	Manual	Auto	Manual	Auto	Manual
Total Study Area (km²)	2.09E+09		1.38E+09		1.34E+09		4.19E+09	
No. Landslides	959	763	1536	1154	386	267	2289	1673
Total Landslide Area (km²)	9.43E+06	1.24E+07	2.12E+07	2.46E+07	3.68E+06	4.07E+06	2.83E+07	3.31E+07
Areal Density	0.005	0.006	0.015	0.018	0.003	0.003	0.007	0.008
Landslide Area % Greater than 10⁵ m²	12.2	16.2	21.6	29.2	9.7	11.1	19.7	25.8
No. Landslides >10⁵ m²	6	8	13	19	2	2	18	23
% of Total Landslide Area from Landslides 3600 m² (4 pixels) or Less	10.6	3.0	6.2	1.9	10.2	4.1	7.5	2.3

Table S1. Description of Landslide Inventory.

Table S2. Description and Ranges of 15 Features

Name	Abbreviation	Units	N-S: Minimum	N-S: Maximum	NW-SE: Minimum	NW-SE: Maximum	E-W: Minimum	E-W: Maximum	Description	Reference
Aspect	Asp	Degrees	0	359.99	0	359.99	0	359.99	Aspect as the direction of slope faces. 0 and 180 represents north and south facing slopes, respectively.	Schwanghart and Scherler, 2014
Curvature (Mean)	Cur _M	m ⁻¹	-0.012	0.010	-0.016	0.010	-0.011	0.009	Curvature for the average of normal sections	
Curvature (Planform)	Cur _{Plan}	m ⁻¹	-7.4	8.7	-7.4	4.8	-2.5	2.6	Curvature perpendicular to slope gradient.	Shary, 1995
Curvature (Profile)	Cur _{Prof}	m ⁻¹	-0.037	0.034	-0.062	0.034	-0.047	0.030	Curvature in the direction of greatest rate of change of slope gradient.	
Curvature (Total)	Cur _{Tot}	m ⁻²	4.2E-10	4.3E-03	1.9E-10	5.8E-03	4.6E-10	4.5E-03	Curvature of the surface itself instead of a line across the surface.	Wilson and Gallant, 2000
Discharge	Discharge	m ³ /yr	1.2E+06	1.8E+13	2.4E+06	2.0E+13	5.4E+05	2.4E+13	The amount of water discharge from upstream areas considering spatially varying MAP. Calculation is based on a D8 flow direction.	Schwanghart and Scherler, 2014
Distance to Channel	Dist _C	m	0	1984	0	2079	0	1892	Distance to channel points defined as drainage area > 1 km ²	Schwanghart and Scherler, 2014
Drainage Area	Drainage Area	m ²	900	8.9E+09	900	9.4E+09	900	1.2E+10	Total area of upstream cells based on a D8 flow direction.	
Elevation	Elev	m	265	4249	229	4106	282	4446	Elevation acquired from a 90 m SRTM DEM.	USGS EarthExplorer
Fault Distance from All Faults	Dist _f	m	0	21831	0	7860	0	15892	Euclidean Distance from faults shown in the lithology map from Haproff et al. (2019).	Haproff et al., 2019
Fault Distance from Main Frontal Thrust/Suture Zone	Dist _{MFT}	m	0	66388	0	31213	4428.3	57076	Euclidean Distance from the main frontal thrust fault and suture shown in the Himalayan fault map from Taylor and Yin (2009).	Taylor and Yin, 2009
Local Relief	Relief	m	97	2772	268	2522	606	2533	Local relief calculated as an elevation range within a 2500m radius circular window	Schwanghart and Scherler, 2014
Mean Annual Precipitation	MAP	mm/yr	1364	7253	2654	7529	600	6954	12 year (1998 - 2009) averaged mean annual precipitation obtained from the Tropical Rainfall Measuring Mission (TRMM).	Bookhagen and Burbank, 2010
Number of Extreme Events	NEE	events/yr	6.8	13.2	9.9	14.1	3.8	12.2	12 year (1998 - 2009) averaged number of extreme events obtained from TRMM.	
Slope	Slope	--	0.1	3.2	0.1	3.3	0.1	3.0	Slope calculated as the steepest descent using D8 flow routing	Schwanghart and Scherler, 2014

Table S2. Description and Ranges of 15 Features.

Table S3. AUROC of Models and Single Features

Models / Features	Area Under the Curve		
	N-S	NW-SE	E-W
<i>SNN</i>			
Single - 1	0.864	0.826	0.878
Composite - 2	0.896	0.856	0.919
Composite - 3	--	0.866	--
<i>Artificial Neural Network (ANN)</i>	0.837	0.762	0.835
<i>Statistical Models</i>			
Logistic Regression	0.869	0.795	0.880
Likelihood Ratio	0.841	0.792	0.835
<i>Physical Models</i>			
Failure Index	0.756	0.694	0.732
Failure Index (<10 ⁵ m ²)	0.784	0.741	0.723
Wetness	0.575	0.516	0.568
<i>Single Features</i>			
Aspect	0.553	0.546	0.588
Curvature (Mean)	0.554	0.534	0.530
Curvature (Planform)	0.537	0.528	0.505
Curvature (Profile)	0.528	0.515	0.526
Curvature (Total)	0.568	0.573	0.611
Discharge	0.504	0.503	0.505
Distance to Channel	0.505	0.523	0.574
Drainage Area	0.502	0.502	0.502
Elevation	0.589	0.513	0.624
Fault Distance from All Faults	0.700	0.544	0.661
Fault Distance from Main Frontal			
Thrust/Suture Zone	0.744	0.603	0.666
Local Relief	0.571	0.525	0.507
Mean Annual Precipitation	0.756	0.525	0.598
Number of Extreme Events	0.744	0.585	0.627
Slope	0.698	0.696	0.760

Table S3. AUROC of Models and Single Features. Entries in italics have negative correlations with landslide propensity AUROC of physical models and single features were normalized to be from 0 to 1 Based on 30% testing partition.

Table S4. Artificial Neural Network and Statistical Model Confidence Intervals

	N-S				NW-SE				E-W			
	SNN	ANN (1st order)	Logistic Regression	Likelihood Ratio	SNN	ANN (1st order)	Logistic Regression	Likelihood Ratio	SNN	ANN (1st order)	Logistic Regression	Likelihood Ratio
Mean	0.900	0.838	0.869	0.843	0.8600	0.762	0.794	0.792	0.92	0.834	0.879	0.834
SE	0.09%	0.26%	0.24%	0.32%	0.11%	0.33%	0.40%	0.35%	0.11%	0.47%	0.50%	0.56%
σ	0.0028	0.0008	0.0008	0.0010	0.0034	0.0010	0.0012	0.0011	0.0035	0.0015	0.0016	0.0018
95% Confidence Interval of Mean												
CI +	0.902	0.840	0.871	0.845	0.862	0.765	0.797	0.794	0.923	0.837	0.882	0.838
CI -	0.898	0.836	0.867	0.841	0.858	0.760	0.791	0.789	0.917	0.830	0.875	0.830
$\pm 2\sigma$ Data Range												
Mean +2 σ	0.906	0.843	0.874	0.850	0.867	0.769	0.802	0.799	0.927	0.843	0.889	0.845
Mean -2 σ	0.894	0.833	0.864	0.837	0.853	0.756	0.786	0.785	0.913	0.824	0.869	0.823

*Based on 10-fold validation of randomly selecting 50% of the 30% testing partition

Table S4. Artificial Neural Network and Statistical Model Confidence Intervals.

Table S5. Performance Metrics

	N-S				NW-SE				E-W							
	SNN-L2	SNN-L1	ANN	LogReg	LR	SNN-L3	SNN-L2	SNN-L1	ANN	LogReg	LR	SNN-L2	SNN-L1	ANN	LogReg	LR
AUROC	0.896	0.864	0.837	0.869	0.841	0.866	0.856	0.826	0.762	0.795	0.792	0.919	0.878	0.835	0.880	0.835
AUROC Manual	0.867	0.828	0.807	0.834	0.824	0.823	0.817	0.784	0.714	0.750	0.740	0.902	0.865	0.798	0.855	0.821
Success Rate AUC	0.895	0.862	0.836	0.867	0.840	0.861	0.850	0.821	0.758	0.790	0.788	0.918	0.877	0.834	0.879	0.834
Accuracy	0.792	0.757	0.727	0.766	0.723	0.810	0.792	0.755	0.697	0.739	0.703	0.838	0.779	0.753	0.812	0.768
True positive Rate/Sensitivity/POD	0.853	0.812	0.787	0.806	0.802	0.770	0.777	0.755	0.682	0.694	0.730	0.867	0.797	0.785	0.794	0.749
False Positive Rate/Specificity/POFD	0.208	0.244	0.274	0.234	0.277	0.189	0.208	0.245	0.303	0.260	0.297	0.162	0.221	0.247	0.188	0.232
POD - POFD	0.644	0.569	0.513	0.572	0.525	0.581	0.569	0.510	0.379	0.434	0.433	0.706	0.576	0.539	0.606	0.517

*Based on 30% testing partition

Table S5. Performance Metrics.

Table S6a. Correlation Metrics Between Features (R-value) (N-S Region)

Features	Asp	Curv _M	Dist _C	Elev	Log ₁₀ (Discharge)	Log ₁₀ (Drainage Area)	Dist _F	Dist _{MFT}	Relief	NEE	MAP	Slope
Asp	1											
Curv _M	-0.002	1										
Dist _C	-0.003	0.290	1									
Elev	0.004	0.154	0.390	1								
Log ₁₀ (Discharge)	0.009	-0.671	-0.327	-0.232	1							
Log ₁₀ (Drainage Area)	0.003	-0.581	-0.210	-0.104	0.696	1						
Dist _F	-0.016	0.001	-0.039	0.179	-0.168	-0.008	1					
Dist _{MFT}	-0.031	-0.001	-0.049	0.382	-0.206	0.005	0.684	1				
Relief	0.036	-0.002	0.045	0.365	0.072	0.041	-0.170	-0.032	1			
NEE	0.010	0.002	0.045	-0.349	0.213	0.009	-0.601	-0.792	0.131	1		
MAP	0.005	-0.00001	0.048	-0.183	0.246	0.007	-0.599	-0.828	0.159	0.802	1	
Slope	-0.015	0.414	0.205	0.167	-0.326	-0.238	-0.110	-0.070	0.311	0.124	0.111	1

Table S6b. Correlation Metrics Between Features (R-value) (NW-SE Region)

Features	Asp	Curv _M	Dist _C	Elev	Log ₁₀ (Discharge)	Log ₁₀ (Drainage Area)	Dist _F	Dist _{MFT}	Relief	NEE	MAP	Slope
Asp	1											
Curv _M	-0.002	1										
Dist _C	-0.028	0.272	1									
Elev	0.013	0.164	0.425	1								
Log ₁₀ (Discharge)	-0.013	-0.686	-0.332	-0.102	1							
Log ₁₀ (Drainage Area)	-0.007	-0.584	-0.199	-0.098	0.717	1						
Dist _F	0.030	0.0001	-0.006	0.165	0.049	0.024	1					
Dist _{MFT}	-0.041	-0.007	-0.008	0.432	0.120	0.054	0.366	1				
Relief	0.032	-0.005	0.018	0.463	0.103	0.048	0.112	0.351	1			
NEE	-0.013	0.003	0.016	0.124	0.037	-0.003	0.032	-0.128	0.177	1		
MAP	-0.024	-0.003	0.034	0.586	0.148	0.030	0.203	0.403	0.485	0.357	1	
Slope	0.023	0.410	0.141	0.188	-0.329	-0.230	0.011	0.053	0.296	0.108	0.168	1

Table S6c. Correlation Metrics Between Features (R-value) (E-W Region)

Features	Asp	Curv _M	Dist _C	Elev	Log ₁₀ (Discharge)	Log ₁₀ (Drainage Area)	Dist _F	Dist _{MFT}	Relief	NEE	MAP	Slope
Asp	1											
Curv _M	-0.001	1										
Dist _C	0.004	0.286	1									
Elev	0.005	0.120	0.336	1								
Log ₁₀ (Discharge)	0.000	-0.686	-0.342	-0.264	1							
Log ₁₀ (Drainage Area)	0.001	-0.595	-0.212	-0.068	0.707	1						
Dist _F	0.029	-0.001	0.013	0.501	-0.092	0.004	1					
Dist _{MFT}	-0.036	-0.009	0.018	0.636	-0.140	0.054	0.330	1				
Relief	-0.051	0.003	0.050	0.312	-0.061	0.040	0.137	0.537	1			
NEE	0.019	0.011	0.009	-0.601	0.194	-0.041	-0.348	-0.786	-0.421	1		
MAP	0.018	0.008	-0.021	-0.553	0.209	-0.042	-0.305	-0.835	-0.426	0.857	1	
Slope	-0.023	0.449	0.210	0.171	-0.421	-0.269	0.053	0.150	0.252	-0.135	-0.117	1

Table S6. Correlation Metrics Between Features.

Table S7. Logistic Regression Control Coefficients

Feature	Coefficient		
	N-S	NW-SE	E-W
Intercept	-13.33	-11.85	-7.09
Asp NE	0.728	0.984	2.166
Asp E	1.626	1.942	3.340
Asp SE	2.510	2.281	3.658
Asp S	2.476	2.264	3.783
Asp SW	2.062	2.104	2.811
Asp W	1.319	1.176	1.834
Asp NW	0.604	-0.286	-0.865
Curv _M	-280	-289	-225
Log ₁₀ (Discharge)	0.055	0.146	-0.092
Dist _C	2.25E-04	2.51E-04	1.12E-03
Log ₁₀ (Drainage Area)	0.008	-0.005	0.096
Elev	-4.48E-04	2.56E-04	-6.60E-04
Dist _F	-1.49E-04	1.38E-04	-2.88E-05
Dist _{MFT}	1.93E-06	-1.16E-04	-6.44E-05
Relief	3.96E-05	2.40E-05	4.96E-04
MAP	2.84E-04	1.03E-05	-1.84E-04
NEE	0.347	0.276	-0.120
Slope	2.383	2.925	3.617

Table S7. Correlation Metrics Between Features.

x_1	x_2	x_3	x_4	$x_1 * x_2$	$x_3 * x_4$	$x_1 * x_2 * x_3 * x_4$	y
0	0	0	0	0	0	0	0
0	0	0	1	0	0	0	0
0	0	1	0	0	0	0	0
0	0	1	1	0	1	0	1
0	1	0	0	0	0	0	0
0	1	0	1	0	0	0	0
0	1	1	0	0	0	0	0
0	1	1	1	0	1	0	1
1	0	0	0	0	0	0	0
1	0	0	1	0	0	0	0
1	0	1	0	0	0	0	0
1	0	1	1	0	1	0	1
1	1	0	0	1	0	0	1
1	1	0	1	1	0	0	1
1	1	1	0	1	0	0	1
1	1	1	1	1	1	1	0

Table S8. Truth table.

Feature	Level
$x1$	1
$x2$	1
$x3$	1
$x4$	1
$x1 * x2$	2
$x1 * x3$	2
$x1 * x4$	2
$x2 * x3$	2
$x2 * x4$	2
$x3 * x4$	2
$x1 * x2 * x3$	3
$x1 * x2 * x4$	3
$x1 * x3 * x4$	3
$x2 * x3 * x4$	3
$x1 * x2 * x3 * x4$	4

Table S9. Composite features.

References

- Adadi, A., & Berrada, M. (2018). Peeking inside the black-box: A survey on explainable artificial intelligence (xai). *IEEE Access*, 6, 52138–52160.
- Agarwal, R., Frosst, N., Zhang, X., Caruana, R., & Hinton, G. (2020). Neural additive models: Interpretable machine learning with neural nets. *arXiv preprint arXiv:2004.13912*.
- Akgun, A. (2012). A comparison of landslide susceptibility maps produced by logistic regression, multi-criteria decision, and likelihood ratio methods: a case study at izmir, turkey. *Landslides*, 9(1), 93–106.
- Barros, A., Kim, G., Williams, E., & Nesbitt, S. (2004). Probing orographic controls in the Himalayas during the monsoon using satellite imagery. *Natural Hazards and Earth System Science, Copernicus Publications on behalf of the European Geosciences Union*, 4.
- Battiti, R. (1992). First- and second-order methods for learning: Between steepest descent and newton’s method. *Neural Computation*, 4(2), 141-166. doi: 10.1162/neco.1992.4.2.141
- Baum, R., Godt, J., & Savage, W. (2010). Estimating the timing and location of shallow rainfall-induced landslides using a model for transient, unsaturated infiltration. *Journal of Geophysical Research: Earth Surface*, 115(F3).
- Baum, R., Savage, W., & Godt, J. (2002). TRIGRS—a Fortran program for transient rainfall infiltration and grid-based regional slope-stability analysis. *US geological survey open-file report*, 424, 38.
- Ben-Menahem, A., Aboodi, E., & Schild, R. (1974). The source of the great Assam earthquake—an interplate wedge motion. *Physics of the Earth and Planetary Interiors*, 9(4), 265-289.
- Bergen, K., Johnson, P., Maarten, V., & Beroza, G. (2019). Machine learning for data-driven discovery in solid earth geoscience. *Science*, 363(6433).
- Beven, K., & Kirkby, M. (1979). A physically based, variable contributing area model of basin hydrology. *Hydrological Sciences Journal*, 24(1), 43–69.
- Bookhagen, B. (2010). Appearance of extreme monsoonal rainfall events and their impact on erosion in the Himalaya. *Geomatics, Natural Hazards and Risk*, 1(1), 37-50.
- Bookhagen, B., & Burbank, D. (2010). Toward a complete Himalayan hydrological budget: Spatiotemporal distribution of snowmelt and rainfall and their impact on river discharge. *Journal of Geophysical Research: Earth Surface*, 115(F3).
- Bouchard, L.-S., & Youssef, K. (2018, April 24). *Feature-preserving noise removal*. Google Patents. (US Patent 9,953,246)
- Burgess, W., Yin, A., Dubey, C., Shen, Z.-K., & Kelty, T. (2012). Holocene shortening across the Main Frontal Thrust zone in the eastern Himalaya. *Earth and Planetary Science Letters*, 357, 152–167.
- Chowdhuri, I., Pal, S., Chakraborty, R., Malik, S., Das, B., & Roy, P. (2021). Torrential rainfall-induced landslide susceptibility assessment using machine learning and statistical methods of eastern himalaya. *Natural Hazards*, 1–26.
- Conforti, M., Pascale, S., Robustelli, G., & Sdao, F. (2014). Evaluation of prediction capability of the artificial neural networks for mapping landslide susceptibility in the turbolo river catchment (northern calabria, italy). *CATENA*, 113, 236 - 250.
- Coudurier-Curveur, A., Tapponnier, P., Okal, E., Van der Woerd, J., Kali, E., Choudhury, S., ... Karakaş, Ç. (2020). A composite rupture model for the great 1950 Assam earthquake across the cusp of the East Himalayan Syntaxis. *Earth and Planetary Science Letters*, 531, 115928.
- Cui, Y., Cheng, D., Choi, C., Jin, W., Lei, Y., & Kargel, J. (2019). The cost of rapid and haphazard urbanization: lessons learned from the freetown landslide disaster. *Landslides*, 16(6), 1167–1176.

- Devkota, K., Regmi, A., Pourghasemi, H., Yoshida, K., Pradhan, B., Ryu, I., . . . Althuwaynee, O. (2013). Landslide susceptibility mapping using certainty factor, index of entropy and logistic regression models in GIS and their comparison at mugling–narayanghat road section in Nepal Himalaya. *Natural Hazards*, *65*(1), 135–165.
- Dietrich, W., Bellugi, D., & Real De Asua, R. (2001). Validation of the shallow landslide model, SHALSTAB, for forest management. *Water Science and Application*, *2*, 195–227.
- Dietrich, W., Reiss, R., Hsu, M., & Montgomery, D. (1995). A process-based model for colluvial soil depth and shallow landsliding using digital elevation data. *Hydrological Processes*, *9*(3-4), 383–400.
- Dikshit, A., Pradhan, B., & Alamri, A. M. (2020). Pathways and challenges of the application of artificial intelligence to geohazards modelling. *Gondwana Research*.
- European Commission. (2020). White paper on artificial intelligence—a European approach to excellence and trust.
- Fan, X., Scaringi, G., Korup, O., West, A., van Westen, C., Tanyas, H., . . . Huang, R. (2019). Earthquake-induced chains of geologic hazards: Patterns, mechanisms, and impacts. *Reviews of Geophysics*, *57*(2), 421–503.
- Fernandes, F., & Lona, L. (2005). Neural network applications in polymerization processes. *Brazilian Journal of Chemical Engineering*, *22*(3), 401–418.
- Friedman, J. (2001). Greedy function approximation: a gradient boosting machine. *Annals of Statistics*, 1189–1232.
- Froude, M., & Petley, D. (2018). Global fatal landslide occurrence from 2004 to 2016. *Natural Hazards and Earth System Sciences*, *18*(8), 2161–2181.
- Ghorbanzadeh, O., Blaschke, T., Gholamnia, K., Meena, S., Tiede, D., & Aryal, J. (2019). Evaluation of different machine learning methods and deep-learning convolutional neural networks for landslide detection. *Remote Sensing*, *11*(2), 196.
- Gómez, H., & Kavzoglu, T. (2005). Assessment of shallow landslide susceptibility using artificial neural networks in Jabonosa river basin, Venezuela. *Engineering Geology*, *78*(1), 11–27. Retrieved from <http://www.sciencedirect.com/science/article/pii/S0013795204002236>
- Gunning, D., Stefik, M., Choi, J., Miller, T., Stumpf, S., & Yang, G.-Z. (2019). XAI—explainable artificial intelligence. *Science Robotics*, *4*(37). doi:10.1126/scirobotics.aay7120
- Guzzetti, F., Carrara, A., Cardinali, M., & Reichenbach, P. (1999). Landslide hazard evaluation: a review of current techniques and their application in a multi-scale study, Central Italy. *Geomorphology*, *31*(1-4), 181–216.
- Haproff, P., Odlum, M., Zuza, A., Yin, A., & Stockli, D. (2020). Structural and thermochronologic constraints on the Cenozoic tectonic development of the northern Indo-Burma Ranges. *Tectonics*, *39*, e2020TC006231.
- Haproff, P., Zuza, A., Yin, A., Harrison, T., Manning, C., Dubey, C., . . . Chen, J. (2019). Geologic framework of the northern Indo-Burma ranges and lateral correlation of Himalayan-Tibetan lithologic units across the eastern Himalayan syntaxis. *Geosphere*, *15*(3), 856–881.
- Hastie, T., & Tibshirani, R. (1990). *Generalized additive models* (Vol. 43). CRC press.
- Hinton, G., Vinyals, O., & Dean, J. (2015). Distilling the knowledge in a neural network. *arXiv:1503.02531*.
- Hooker, G. (2004). Discovering additive structure in black box functions. In *Proceedings of the tenth ACM SIGKDD international conference on knowledge discovery and data mining* (pp. 575–580).
- Huang, A.-L., & Montgomery, D. (2014). Topographic locations and size of earthquake- and typhoon-generated landslides, Tachia river, Taiwan. *Earth*

- Surface Processes and Landforms*, 39(3), 414–418.
- Huang, R., & Fan, X. (2013). The landslide story. *Nature Geoscience*, 6(5), 325–326.
- Iverson, R. (2000). Landslide triggering by rain infiltration. *Water resources research*, 36(7), 1897–1910.
- Kavzoglu, T., Sahin, E., & Colkesen, I. (2014). Landslide susceptibility mapping using GIS-based multi-criteria decision analysis, support vector machines, and logistic regression. *Landslides*, 11(3), 425–439.
- Kent, W., & Dasgupta, U. (2004). Structural evolution in response to fold and thrust belt tectonics in northern Assam. a key to hydrocarbon exploration in the Jaipur anticline area. *Marine and Petroleum Geology*, 21(7), 785–803.
- Kingma, D., & Ba, J. (2014). Adam: A method for stochastic optimization. *arXiv preprint arXiv:1412.6980*.
- Kirschbaum, D., Kapnick, S., Stanley, T., & Pascale, S. (2020). Changes in extreme precipitation and landslides over high mountain asia. *Geophysical Research Letters*, 47(4), e2019GL085347.
- Krizhevsky, A., Sutskever, I., & Hinton, G. (2012). Imagenet classification with deep convolutional neural networks. In *Advances in neural information processing systems* (p. 1097–1105).
- Larsen, I., & Montgomery, D. (2012). Landslide erosion coupled to tectonics and river incision. *Nature Geoscience*, 5(7), 468–473.
- Larsen, I., Montgomery, D., & Korup, O. (2010). Landslide erosion controlled by hillslope material. *Nature Geoscience*, 3(4), 247–251.
- Lawrence, S., Giles, C., Tsoi, A., & Back, A. (1997). Face recognition: A convolutional neural-network approach. *IEEE transactions on neural networks*, 8(1), 98–113.
- Le, Q., Ngiam, J., Coates, A., Lahiri, A., Prochnow, B., & Ng, A. (2011). On optimization methods for deep learning. In *Proceedings of the 28 th international conference on machine learning, bellevue, wa, usa* (p. 265–272).
- Lee, S. (2005). Application of logistic regression model and its validation for landslide susceptibility mapping using GIS and remote sensing data. *International Journal of Remote Sensing*, 26(7), 1477–1491.
- Lee, S., Ryu, J.-H., Won, J.-S., & Park, H.-J. (2004). Determination and application of the weights for landslide susceptibility mapping using an artificial neural network. *Engineering Geology*, 71(3–4), 289–302.
- Lee, S., & Sambath, T. (2006). Landslide susceptibility mapping in the Damrei Romel area, Cambodia using frequency ratio and logistic regression models. *Environmental Geology*, 50(6), 847–855.
- Leonarduzzi, E., Maxwell, R., Mirus, B. B., & Molnar, P. (2021). Numerical analysis of the effect of subgrid variability in a physically based hydrological model on runoff, soil moisture, and slope stability. *Water Resources Research*, 57(4), e2020WR027326.
- Li, X.-H., Cao, C., Shi, Y., Bai, W., Gao, H., Qiu, L., . . . Chen, L. (2020). A survey of data-driven and knowledge-aware eXplainable AI. *IEEE Transactions on Knowledge and Data Engineering*.
- Mandal, S., & Mandal, K. (2018). Modeling and mapping landslide susceptibility zones using GIS based multivariate binary logistic regression (LR) model in the Rorachu river basin of eastern Sikkim Himalaya, India. *Modeling Earth Systems and Environment*, 4(1), 69–88.
- Marc, O., & Hovius, N. (2015). Amalgamation in landslide maps: effects and automatic detection. *Natural Hazards & Earth System Sciences*, 15(4).
- McGuire, L., Rengers, F., Kean, J., Coe, J., Mirus, B., Baum, R., & Godt, J. (2016). Elucidating the role of vegetation in the initiation of rainfall-induced shallow landslides: Insights from an extreme rainfall event in the Colorado front range. *Geophysical Research Letters*, 43(17), 9084–9092.

- Meunier, P., Hovius, N., & Haines, J. (2008a). Topographic site effects and the location of earthquake induced landslides. *Earth and Planetary Science Letters*, 275(3-4), 221-232.
- Meunier, P., Hovius, N., & Haines, J. (2008b). Topographic site effects and the location of earthquake induced landslides. *Earth and Planetary Science Letters*, 275(3-4), 221-232.
- Montavon, G., Orr, G., & Müller, K.-R. (2012). *Neural Networks: Tricks of the Trade* (Vol. 7700). Springer.
- Montgomery, D., & Dietrich, W. (1994). A physically based model for the topographic control on shallow landsliding. *Water Resources Research*, 30(4), 1153-1171.
- Montgomery, D., Sullivan, K., & Greenberg, H. (1998). Regional test of a model for shallow landsliding. *Hydrological processes*, 12(6), 943-955.
- Moon, S., Chamberlain, C., Blisniuk, K., Levine, N., Rood, D., & Hilley, G. (2011). Climatic control of denudation in the deglaciated landscape of the Washington Cascades. *Nature Geoscience*, 4(7), 469-473.
- Orland, E., Roering, J., Thomas, M., & Mirus, B. (2020). Deep learning as a tool to forecast hydrologic response for landslide-prone hillslopes. *Geophysical Research Letters*, 47(16), e2020GL088731. doi: 10.1029/2020GL088731
- Ozyildirim, B., & Kiran, M. (2020). Do optimization methods in deep learning applications matter? *arXiv:2002.12642*.
- Parker, R., Densmore, A., Rosser, N., De Michele, M., Li, Y., Huang, R., . . . Petley, D. (2011). Mass wasting triggered by the 2008 wenchuan earthquake is greater than orogenic growth. *Nature Geoscience*, 4(7), 449-452.
- Petley, D. (2012). Global patterns of loss of life from landslides. *Geology*, 40(10), 927-930.
- Phong, T., Phan, T., Prakash, I., Singh, S., Shirzadi, A., Chapi, K., . . . Pham, B. (2019). Landslide susceptibility modeling using different artificial intelligence methods: A case study at Muong Lay district, Vietnam. *Geocarto International*, 1-24.
- Pradhan, B. (2013). A comparative study on the predictive ability of the decision tree, support vector machine and neuro-fuzzy models in landslide susceptibility mapping using GIS. *Computers & Geosciences*, 51, 350-365.
- Prakash, N., Manconi, A., & Loew, S. (2020). Mapping landslides on eo data: Performance of deep learning models vs. traditional machine learning models. *Remote Sensing*, 12(3), 346.
- Radbruch-Hall, D. H. (1982). *Landslide overview map of the conterminous united states* (Vol. 1183). US Government Printing Office.
- Regmi, A., Devkota, K., Yoshida, K., Pradhan, B., Pourghasemi, H., Kumamoto, T., & Akgun, A. (2014). Application of frequency ratio, statistical index, and weights-of-evidence models and their comparison in landslide susceptibility mapping in central Nepal Himalaya. *Arabian Journal of Geosciences*, 7(2), 725-742.
- Reichenbach, P., Rossi, M., Malamud, B., Mihir, M., & Guzzetti, F. (2018). A review of statistically-based landslide susceptibility models. *Earth-Science Reviews*, 180, 60-91.
- Rudin, C. (2019). Stop explaining black box machine learning models for high stakes decisions and use interpretable models instead. *Nature Machine Intelligence*, 1(5), 206-215.
- Salvi, D., Mathew, G., Kohn, B., Pande, K., & Borgohain, B. (2020). Thermochronological insights into the thermotectonic evolution of Mishmi Hills across the Dibang Valley, NE Himalayan Syntaxis. *Journal of Asian Earth Sciences*, 190, 104158.
- Scherler, D., Bookhagen, B., & Strecker, M. (2014). Tectonic control on ^{10}Be -derived erosion rates in the Garhwal Himalaya, India. *Journal of Geophysical Research*:

- Earth Surface*, 119(2), 83-105.
- Schmidt, J., Evans, I., & Brinkmann, J. (2003). Comparison of polynomial models for land surface curvature calculation. *International Journal of Geographical Information Science*, 17(8), 797-814.
- Schwanghart, W., & Scherler, D. (2014). TopoToolbox 2—MATLAB-based software for topographic analysis and modeling in Earth surface sciences. *Earth Surface Dynamics*, 2(1), 1-7.
- Stanley, T., & Kirschbaum, D. B. (2017). A heuristic approach to global landslide susceptibility mapping. *Natural hazards*, 87(1), 145–164.
- Stine, R. (1995). Graphical interpretation of variance inflation factors. *The American Statistician*, 49(1), 53-56.
- Stock, J., & Dietrich, W. (2003). Valley incision by debris flows: Evidence of a topographic signature. *Water Resources Research*, 39(4).
- Stock, J., & Dietrich, W. (2006). Erosion of steepland valleys by debris flows. *Geological Society of America Bulletin*, 118(9-10), 1125–1148.
- Tan, H., & Lim, K. (2019, jun). Review of second-order optimization techniques in artificial neural networks backpropagation. *IOP Conference Series: Materials Science and Engineering*, 495, 012003.
- Tan, S., Caruana, R., Hooker, G., Koch, P., & Gordo, A. (2018). Learning global additive explanations for neural nets using model distillation. *arXiv:1801.08640*.
- Taylor, M., & Yin, A. (2009). Active structures of the Himalayan-Tibetan orogen and their relationships to earthquake distribution, contemporary strain field, and Cenozoic volcanism active structures on the Tibetan Plateau and surrounding regions. *Geosphere*, 5(3), 199-214.
- Tien Bui, D., Pradhan, B., Lofman, O., Revhaug, I., & Dick, O. (2012). Landslide susceptibility assessment in the hoa binh province of vietnam: a comparison of the levenberg–marquardt and bayesian regularized neural networks. *Geomorphology*, 171, 12–29.
- Tien Bui, D., Shahabi, H., Omidvar, E., Shirzadi, A., Geertsema, M., Clague, J., ... Lee, S. (2019). Shallow landslide prediction using a novel hybrid functional machine learning algorithm. *Remote Sensing*, 11(8), 931.
- Tien Bui, D., Tsangaratos, P., Nguyen, V.-T., Van Liem, N., & Trinh, P. (2020). Comparing the prediction performance of a deep learning neural network model with conventional machine learning models in landslide susceptibility assessment. *Catena*, 188, 104426.
- Toms, B., Barnes, E., & Ebert-Uphoff, I. (2020). Physically interpretable neural networks for the geosciences: Applications to earth system variability. *Journal of Advances in Modeling Earth Systems*, 12(9), e2019MS002002.
- Tucker, C., Fung, I., Keeling, C., & Gammon, R. (1986). Relationship between atmospheric CO₂ variations and a satellite-derived vegetation index. *Nature*, 319(6050), 195–199.
- United States Geological Survey EarthExplorer. (2020). *accessed September 26, 2020, <https://earthexplorer.usgs.gov/>*.
- Van Dao, D., Jaafari, A., Bayat, M., Mafi-Gholami, D., Qi, C., Moayedi, H., ... Trinh, P. (2020). A spatially explicit deep learning neural network model for the prediction of landslide susceptibility. *Catena*, 188, 104451.
- Wilamowski, B., & Yu, H. (2010). Improved computation for Levenberg-Marquardt training. *IEEE transactions on neural networks*, 21(6), 930–937.
- Xu, C., Xu, X., Yao, X., & Dai, F. (2014). Three (nearly) complete inventories of landslides triggered by the May 12, 2008 Wenchuan mw 7.9 earthquake of China and their spatial distribution statistical analysis. *Landslides*, 11(3), 441–461.
- Xu, L., & Zhang, W.-J. (2001). Comparison of different methods for variable selection. *Analytica Chimica Acta*, 446(1-2), 475–481.
- Yang, Y., Zhao, T., Ni, G., & Sun, T. (2018). Atmospheric rivers over the bay of

- bengal lead to northern indian extreme rainfall. *International Journal of Climatology*, 38(2), 1010–1021.
- Yatagai, A., Kamiguchi, K., Arakawa, O., Hamada, A., Yasutomi, N., & Kitoh, A. (2012). APHRODITE: Constructing a long-term daily gridded precipitation dataset for Asia based on a dense network of rain gauges. *Bulletin of the American Meteorological Society*, 93(9), 1401-1415.
- Youssef, K., Bouchard, L.-S., Haigh, K., Silovsky, J., Thapa, B., & Vander Valk, C. (2018a). Machine learning approach to rf transmitter identification. *IEEE Journal of Radio Frequency Identification*, 2(4), 197–205.
- Youssef, K., Bouchard, L.-S., Haigh, K., Silovsky, J., Thapa, B., & Vander Valk, C. (2018b). Machine learning approach to RF transmitter identification. *IEEE Journal of Radio Frequency Identification*, 2(4), 197-205.
- Youssef, K., Jarenwattananon, N., & Bouchard, L.-S. (2015). Feature-preserving noise removal. *IEEE Transactions on Medical Imaging*, 34(9), 1822–1829.
- Yu, H., & Wilamowski, B. (2011). Levenberg-marquardt training. *Industrial electronics handbook*, 5(12), 1.
- Zanter, K. (2016). *Landsat 8 (L8) Data Users Handbook* [Book].
- Zhu, Z., Wulder, M., Roy, D., Woodcock, C., Hansen, M., Radeloff, V., . . . Scambos, T. (2019). Benefits of the free and open landsat data policy. *Remote Sensing of Environment*, 224, 382–385.